Atmospheric Research 325 (2025) 108231

Contents lists available at ScienceDirect

Atmospheric Research

journal homepage: www.elsevier.com/locate/atmosres

Intercomparison of GPM hourly precipitation products: Assessing the strengths in capturing precipitation events and their properties

Meng Cao [a,b,c], Min Chen [a,d,*], Jeffrey Walker [c]

[a] College of Hydraulic & Environmental Engineering, China Three Gorges University, Yichang 443002, China
[b] State Key Laboratory of Hydrology-Water Resources and Hydraulic Engineering, Nanjing Hydraulic Research Institute, Nanjing 210029, China
[c] Department of Civil Engineering, Monash University, Clayton, VIC 3800, Australia
[d] Engineering Research Center of Eco-environment in Three Gorges Reservoir Region, Ministry of Education, Yichang 443002, China

ARTICLE INFO

Keywords:
Satellite precipitation products
GPM
IMERG
GSMaP
Event-based evaluation
Minimum inter-event time

ABSTRACT

Spatially and temporally enhanced satellite precipitation products (SPPs) from the GPM mission offer a viable alternative to ground-based measurements. Although the SPPs have been extensively evaluated at specific time scales, such as hourly and daily, the temporally continuity feature of precipitation events is often overlooked. This study assessed and intercompared the performance of six GPM hourly SSPs, i.e. Early, Late and Final from IMERG, and NRT, MVK, NRT_GC (hereafter GC) from GSMaP, focusing on capturing three key precipitation properties (i.e. depth, duration and intensity) along with peak magnitude and timing, in order to obtain a comprehensive understanding of their capability and potential for precipitation monitoring and related hydrometeorological applications. The minimum inter-event time (MIT) approach, with a range of threshold values (i.e. 1, 2, 6, 10 and 24 h), was adopted to delineate precipitation events for the SSPs and the reference data (site observations and CLDAS datasets). IMERG and GSMaP products revealed their respective strengths in detection capacity of precipitation events, with IMERG achieving lower FAR and GSMaP showing higher POD. Despite comparable capabilities in estimating the depth of precipitation events by all the SPPs, IMERG products tended to be more effective in characterizing precipitation intensity and event peak while GSMaP better identified event duration. Notably, near/post real-time products outperformed gauge-corrected versions in certain aspects. Early was more capable of capturing event-based precipitation properties compared to the other IMERG products, especially for shorter MITs, suggesting the potential of near-real-time products in precipitation monitoring and early warning of associated hazards. In addition, MVK excelled in characterizing event duration, intensity, and peak magnitude within the GSMaP system, revealing the possible effectiveness of gauge-free satellite retrieval algorithms. Subregion analysis using the K-means clustering algorithm demonstrated the integrated influence of multiple factors on the performance of the SPPs, also with region-dependent sensitivity to a specific factor. The findings obtained from this study could provide new insights into the practical application and possible further enhancement of the GPM SPPs.

1. Introduction

With the development of remote sensing technology for precipitation retrieval in recent decades, a series of satellite precipitation products (SPPs) have been released, providing decent spatial and temporal resolutions (Kucera et al., 2013; Li et al., 2021b). The most commonly used SPPs include the Tropical Rainfall Measuring Mission (TRMM; Kummerow, 1993), Climate Prediction Center (CPC) Morphing (CMORPH; Joyce et al., 2004), Precipitation Estimation from Remotely Sensed Information using Artificial Neural Networks (PERSIANN; Hsu et al., 1997), and more recently the Global Precipitation Measurement (GPM) mission with the associated Integrated Multi-satellite Retrievals (IMERG; Hou et al., 2014) and Global Satellite Mapping of Precipitation (GSMaP; Kubota et al., 2007).

The GPM project was designed to deliver a new generation of satellite precipitation product (SPPs) at an enhanced temporal and spatial resolution (half-hourly, 0.1° × 0.1°) with higher accuracy (Hou et al., 2014; Kubota et al., 2007). The two systems of GPM, i.e. IMERG and GSMaP, containing near-real-time, post-real-time and gauge-corrected products, have both been extensively evaluated from regional to

* Corresponding author.
E-mail address: minchen@ctgu.edu.cn (M. Chen).

https://doi.org/10.1016/j.atmosres.2025.108231
Received 4 January 2025; Received in revised form 21 April 2025; Accepted 18 May 2025
Available online 19 May 2025

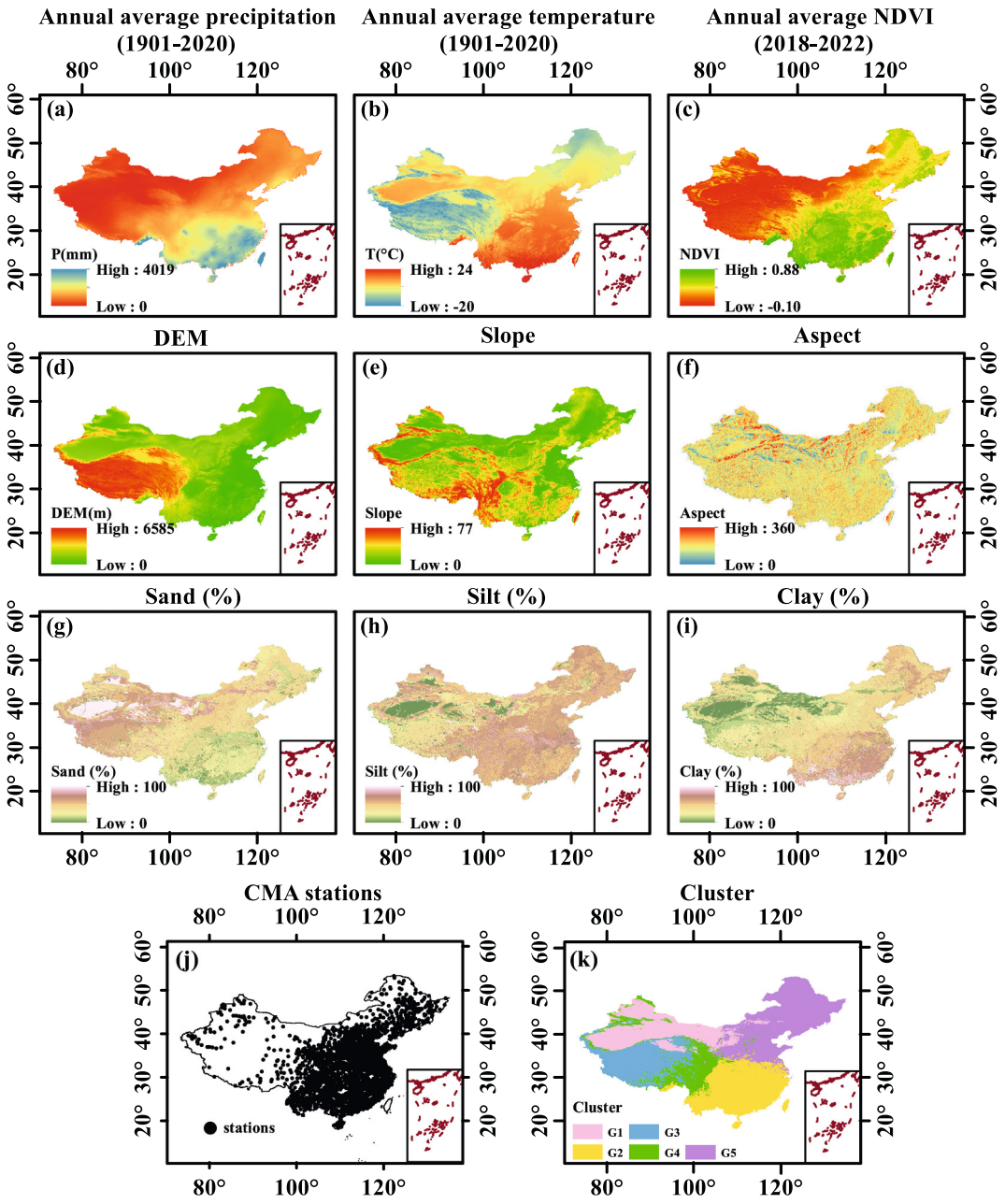

Fig. 1. Maps of climate (a,b), vegetation (c), landscape (d-f) and soil (g-i) properties, rain gauge stations (j) and the subregion delineation results (k) of the study area.

global scales in recent years, demonstrating their effectiveness in monitoring precipitation (time of occurrence and quantity) across a range of spatiotemporal scales (Beck et al., 2017; Pradhan et al., 2022; Zhou et al., 2020). The gauge-corrected versions have generally presented superior performance to the near/post real-time products, especially at larger temporal scales (Lu and Yong, 2018; Pradhan et al., 2022; Yang et al., 2020). Some studies focused on the capacity of SPPs in capturing extreme precipitation events, either for direct evaluation of the precipitation magnitudes (Palharini et al., 2020; Salih et al., 2024; Sharifi et al., 2018), or for the assessment of rainfall-based applications, such as flood forecasting (Quintero et al., 2016; Tapiador et al., 2021; Yuan et al., 2019) and typhoon tracking (Ayat et al., 2021; Roversi et al., 2024; Yu et al., 2021). The GPM SPPs have shown the ability to characterize extreme precipitation events from either perspective (Li et al., 2022; Libertino et al., 2016; Omranian et al., 2018; Shi et al., 2021). Although the evaluation studies of GPM SPPs have enhanced our understanding of their potential capabilities, strengths and limitations (Chen et al., 2020b), most of the validations were implemented at specific time scales (e.g. daily, monthly and annually), with extreme-event analyses also based on precipitation data at a fixed-time interval (e.g. 24 h).

Unlike other environmental variables (e.g. soil moisture, vegetation condition, temperature etc.), precipitation manifests as a discontinuous phenomenon, both spatially and temporally, often adopting the form of "events" characterized by a distinct spatial extent and time span (Tapiador et al., 2019). The occurrence and properties of precipitation is directly related to the thermodynamic and microphysical atmospheric processes operating at the associated scale and the type of precipitation (Berg et al., 2013; Lamjiri et al., 2017; Li et al., 2023). Land surface processes and hazards, such as infiltration, runoff, soil erosion and landslides, are heavily influenced by precipitation events (Blenkinsop et al., 2017; Lewis et al., 2019). Fixed-timescale (e.g. daily) precipitation

Table 1
Summary of the precipitation products and datasets used in this study.

Datasets		Spatial resolution	Temporal resolution	Period	Time latency	Data source
Rain gauge		–	1 h	2019.07–2020.12, 2021.12–2022.09	–	CMA
CLDAS		0.0625°	1 h	2018.01–2022.12	2 days	
IMERG	Early	0.01°	0.5 h	2018.01–2022.12	4 h	NASA
	Late	0.01°	0.5 h	2018.01–2022.12	12 h	
	Final	0.01°	0.5 h	2018.01–2021.09	3.5 month	
GSMaP	NRT	0.01°	1 h	2018.01–2022.12	4 h	JAXA
	MVK	0.01°	1 h	2018.01–2022.12	3 days	
	GC	0.01°	1 h	2018.01–2022.12	4 h	

analysis of the SPPs may overlap multiple distinct precipitation events, while a single precipitation event might span several fixed-time intervals (e.g., hourly) (Dunkerley, 2012; Freitas et al., 2020; Hanel and Maca, 2014). Thus, evaluation of SPPs at a fixed-time scale is inadequate for understanding and analyzing precipitation and its resulting processes. Accordingly, it is necessary to assess the SPPs from an event perspective, which is essential for further application in hydro-meteorological fields. Studies considering event-based evaluation of SPPs originally focused on the simulation of flood events, in which precipitation events were analyzed as basin-scale averages (Mei et al., 2014; Mei et al., 2016; Nikolopoulos et al., 2013). Maranan et al. (2020) then solely targeted at precipitation events and evaluated the ability of the IMERG Final to capture the event duration. Freitas et al. (2020) and Li et al. (2021b) further analyzed the performance of IMERG Final in characterizing precipitation depth, duration and intensity in Brazil and China, respectively. Nevertheless, there remains a lack of studies examining the behavior of SPPs from an event-based perspective, particularly with intercomparisons between different SPPs, which restricts a comprehensive understanding of the capability of each SPP in terms of precipitation event monitoring and associated applications, e.g. forecasts and early warnings of floods and other natural hazards.

The objective of this study is to assess and intercompare the performance of the GPM SPPs (both IMERG and GSMaP) from an event-based perspective, focusing on their capability in detecting precipitation events as well as capturing event properties. The minimum inter-event time (MIT) approach, which has been widely tested to be effective (Dunkerley, 2008, 2012), was employed to delineate precipitation events. A range of MIT values were adopted to analyze the impact of the MIT criteria on the effectiveness of the SPPs. China was selected as the study region due to its complex terrain, diverse climate conditions and variable rainfall patterns, which enables an investigation on influence of various external factors on the performance of the GPM SPPs. This study therefore elucidates the potential of SPPs in monitoring precipitation events and the factors driving good performance, providing a scientific reference for their use in hydrometeorological fields across different climatic and geographical regions.

2. Study area and data

2.1. Study area

The People's Republic of China (hereafter referred to as China), the third-largest country in the world with an area of approximately 9.6×10^6 km^2, is characterized by diverse climate conditions and landscapes. A large number of studies have indicated the potentially substantial impact of climate and underlying land surface conditions on the accuracy of SPPs (Anjum et al., 2018; Chen et al., 2019; Chiaravalloti et al., 2018; Demaria et al., 2011). China is thus suitable for an in-depth evaluation of SPP performance and the external driving factors. The climate in China is predominantly governed by the continental monsoon (Chen et al., 2019; Zhou et al., 2020), which results in a decrease of precipitation from southeast coastal area to northwest inland regions (Fig. 1a). The underlying vegetation condition typically follows the pattern in precipitation, with wetter regions being more densely vegetated (Fig. 1c). Additionally, the elevation progressively rises from the east to the west, culminating in the Tibet Plateau, which is renowned as "the roof of the world" (Fig. 1d), enabling the assessment of SPPs under complex terrain, of which high-altitude regions have been recognized to have relatively poor performance (Chen et al., 2019; Mei et al., 2016).

2.2. Satellite precipitation datasets

The SSPs from the GPM mission are based on the integration of precipitation estimates derived from several passive microwave (PMW) satellites and many geosynchronous microwave-calibrated infrared (IR) sensors within the GPM constellation, using various algorithms. The GPM project features two unique instruments: the Dual-frequency Precipitation Radar (DPR) and the GPM Microwave Imager (GMI), both of which are the most advanced sensors designed for measuring precipitation from space (Hou et al., 2014). The GPM mission encompasses two main systems: the GPM IMERG from the National Aeronautics and Space Administration (NASA) and GSMaP (Kubota et al., 2007) developed by the Japan Aerospace Exploration Agency (JAXA). Both systems provide near/post real-time and gauge-corrected products, respectively. Despite sharing similar input data, differences in the algorithms and the correction procedures lead to varying accuracy levels of these SPPs (Zhou et al., 2020). In this study, six commonly used SPPs from GPM are investigated, being IMERG-Early (hereafter referred to as Early), IMERG-Late (hereafter referred to as Late), IMERG-Final (hereafter referred to as Final), GSMaP-NRT (hereafter referred to as NRT), GSMaP-MVK (hereafter referred to as MVK) and GSMaP-NRT-GC (hereafter referred to as GC). The basic information of these SPPs is summarized in Table 1.

The IMERG suite provides global precipitation at a spatial resolution of $0.1^\circ \times 0.1^\circ$ across multiple temporal resolutions, including half-hourly, daily and monthly. The DPR and GMI are applied to intercalibrate the precipitation traits merged from various PMW for IMERG, while microwave-calibrated IR is used to compute precipitation rate. Finer-resolution precipitation estimates are propagated from the microwave maps utilizing a morphing technique in a forward/backward way. The near real-time "Early Run" (4-h data latency) employs forward-only morphing. Both forward and backward morphing are implemented for the post real-time "Late Run" (12- h data latency) and the gauge-corrected "Final Run" (3.5-month data latency), with the "Final Run" further incorporating monthly GPCC gauge data. All the datasets are freely accessible from https://gpm.nasa.gov/data/directory. This study evaluates the three half-hourly IMERG products (Version 6) for the period 2018 to 2022.

The GSMaP system generates multi-satellite precipitation products with high spatiotemporal resolution (0.1°, hourly) by integrating PMW estimates with partial IR estimates (Chen et al., 2019; Ushio et al., 2009). Unlike IMERG, which employs both DPR and GMI for calibration, DPR is solely adopted to correct the PMW-based precipitation estimates. The MVK product (post-real-time version, 3-days data latency) integrates PMW data with IR brightness temperature, and a Kalman filter (KF) is applied to refine the precipitation rate propagated based on the atmospheric moving vector derived from two successive IR images,

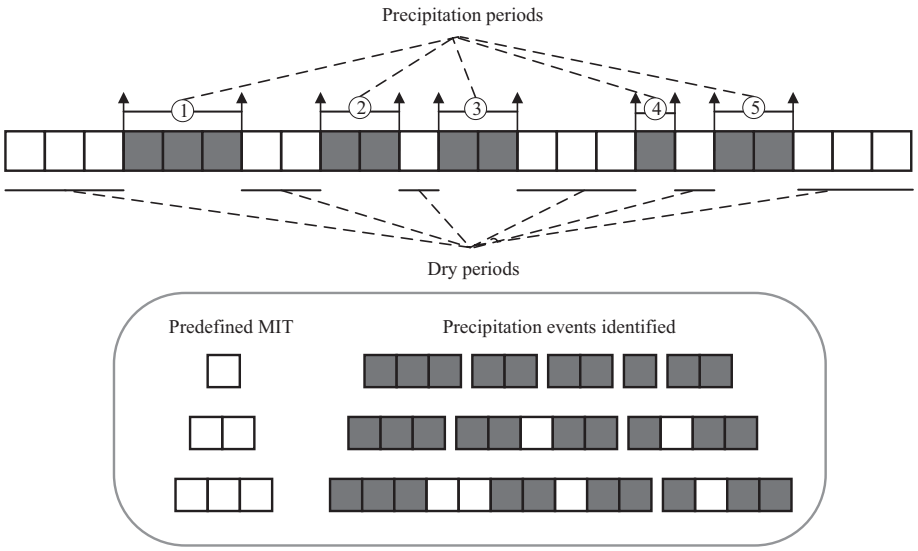

Fig. 2. Definition of precipitation events based on MIT criterion.

while the NRT (near-real-time version, 4-h data latency) is based on a more streamlined algorithmic process. Global gauge-based analysis of daily precipitation from the NOAA Climate Prediction Center (CPC) underpins the gauge-correction products (both for NRT_GC and MVK_GC) in this system (Chen et al., 2008). All the gauge-corrected versions have the same data latency with their uncorrected version (4 h for NRT_GC and 3 days for MVK_GC). In this study, the gauge-corrected version of NRT, i.e. NRT_GC (hereafter for GC), was selected as the representative of the GSMaP gauge-corrected datasets. The hourly NRT, MVK and GC (Version 6) from 2018 to 2022 were used, which are available on the JAXA website (https://sharaku.eorc.jaxa.jp/).

2.3. Gauge observations and CLDAS datasets

Hourly observations from over 2000 automatic weather stations (AWSs) operated by the National Meteorological Information Center of the China Meteorological Administration (CMA) were considered to validate the SPPs, while stations used for originally calibrating these SPPs were excluded to ensure data independency. Rigorous quality control has been conducted over the whole mainland China. Due to data availability, ground records from July 2019 to December 2020 and January to September 2022 were analyzed in this study. The spatial distribution of CMA stations used in this study is presented in Fig. 1j.

Additionally, hourly precipitation datasets from the China Meteorological Administration Land Data Assimilation System (CLDAS) were also employed for the purpose of validation. CLDAS v2.0 integrates data from various sources (e.g. Fengyun-2 series of Chinese geostationary meteorological satellite precipitation, CMORPH and ground-based measurements) via data fusion and assimilation techniques (Shi et al., 2011), providing hourly precipitation over the East Asian region (70–150°E, 0–60°N) at a spatial resolution of 0.0625°. With stringent quality control, the CLDAS dataset has a high level of accuracy, with a bias of only −0.0004 mm/h for the hourly precipitation (China Meteorological Administration, 2017). The CLDAS precipitation data have also been well validated in a large number of studies (Han et al., 2019; Shen et al., 2013; Shen et al., 2014; Sun et al., 2020; Yang et al., 2017). Accordingly, the CLDAS hourly precipitation data from 2018 to 2022 was used in this study.

2.4. Supplementary data

2.4.1. Annual average precipitation and temperature

Annual average precipitation and temperature are key factors delineating climate regions according to the Köppen climate classification. The grid-based monthly climatic datasets (1 km × 1 km) from 1901 to 2020 from the National Tibetan Plateau Data Center (http://data.tpdc.ac.cn/) were used to determine the annual average values for both precipitation and temperature. These datasets combine global climate suites from the Climatic Research Unit (CRU) and WorldClim (https://www.worldclim.org/). Their accuracy has been proven through validation against 496 independent meteorological stations (Peng et al., 2019). The resulting maps of average precipitation and temperature across China are presented in Fig. 1a and Fig. 1b, respectively, showing similar distributions with those calculated by the gauge observations (Tang et al., 2016; Yu et al., 2020).

2.4.2. Land surface properties

Land surface features including vegetation condition, Digital Elevation Model (DEM) -derived characteristics, and soil properties were also utilized for subregion delineation in this study, to analyze driving factors for the performance of the SPPs. The Normalized Difference Vegetation Index (NDVI), effective for monitoring vegetation activity and biomass (Katsiabani et al., 2006; Xu et al., 2015), was adopted as the indicator of underlying surface vegetation condition. Accordingly, the NDVI employed in this study was from the Moderate-Resolution Imaging Spectroradiometer (MODIS) sensor aboard the Terra satellite (https://lpdaac.usgs.gov/), specifically the monthly MOD13C2 NDVI product at a spatial resolution of 0.05° from 2018 to 2022. The 30 m resolution DEM data were from the Shuttle Radar Topography Mission (SRTM) provided by NASA (https://earthdata.nasa.gov/), with slope and aspect subsequently computed. Soil texture was chosen as the indicator of soil properties due to its importance in land clustering and its widespread use in site grouping (Devine et al., 2021; Donoghue et al., 2019; Krueck et al., 2006). Maps of sand, silt and clay percentage (1 km × 1 km) from the Data Center for Resources and Environmental Sciences, Chinese Academy of Sciences (RESDC) (https://www.resdc.cn/) were utilized in this study. A bilinear interpolation resampling method was applied to obtain maps of all these factors at the same spatial resolution as the SPPs.

3. Methodology

3.1. Identification of precipitation events

The minimum inter-event time (MIT) method, which is the most widely used approach to identify individual precipitation events from

successive precipitation records (Dunkerley, 2008; Hanel and Maca, 2014; Molina-Sanchis et al., 2016), was used in this study. This method employs a specified rainless interval to distinguish discrete precipitation events. Specifically, a precipitation event is identified only if the intervening dry period meets or exceeds a predefined threshold (the MIT value), as illustrated in Fig. 2. Given that the choice of MIT criteria could significantly influence the identification results of precipitation events (Dunkerley, 2008, 2015; Dunkerley, 2010), a series of commonly used MIT thresholds (1, 2, 6, 24 h) were selected to divide consecutive rain records. MIT = 1 h and 24 h were selected to represent distinctly different conditions, i.e. relatively short and long separation intervals between events, normally corresponding to short-duration and long-duration precipitation events, respectively. MIT = 2 and 6 h were included since they have been commonly adopted in hydro-meteorological research and practices (Brasil et al., 2022; Hirschberg et al., 2021; He et al., 2022). An MIT value of 10 h was also considered, as suggested by Wang et al. (2019), for its desirable applicability in China.

3.2. Evaluation of the satellite precipitation products

The performance of the six GPM SPPs for identifying the properties of precipitation events were evaluated against both reference datasets, being the gauge observations and grid-scale CLDAS dataset. Pixels of satellite products paired with the ground sites were first identified, and the gauge precipitation data within the same grid was averaged to obtain the "ground truth" for that pixel. For CLDAS, bilinear interpolation was used to match its spatial scale with that of the SSPs, from 0.0625° to 0.01°. A precipitation depth threshold of 2.5 mm was adopted, excluding events with a total depth below this value from the analysis, to reduce the occurrence of false alarms commonly observed in satellite precipitation products for very light rainfall events (Freitas et al., 2020; Bi et al., 2022; Li et al., 2021a, 2021b, 2021c). For comparison, an event identified by both the SPPs and reference data was considered to be the same event if more than 50 % of the event process overlapped, or if the time lag between their centroids was within 2.5 times the MIT value (Freitas et al., 2020).

Three commonly used indices were applied to assess the detectability of each SPP, being probability of detection (POD), false alarm ratio (FAR) and critical success index (CSI) (Freitas et al., 2020; Gadelha et al., 2019; Tang et al., 2016). These indices were calculated according to:

$$POD = \frac{a}{a+c} \tag{1}$$

$$FAR = \frac{b}{a+b} \tag{2}$$

$$CSI = \frac{a}{a+b+c} \tag{3}$$

where a is the number of precipitation events detected by both the reference data and the SPPs; b refers to the number of events falsely captured by the SPPs but did not actually occur; c denotes the number of events detected by the reference data but not captured by the SPPs. The POD and CSI reflect the ability of the SPPs to accurately detect precipitation events, while the FAR indicates the performance of the SPPs in avoiding a false alarm. All three indices range from 0 to 1, with the optimal value being 1 for POD and CSI, and 0 for FAR.

The capability of the SPPs was also assessed in capturing the event-based precipitation properties, consisting of event-wide metrics and peak-related metrics. Event-wide properties include event depth (D, mm), duration (T, h) and intensity (D/T, mm/h). The ratio bias (RB) and mean relative error (MRE) were introduced to evaluate the performance of each SPP in characterizing these three properties, defined as:

$$RB = \frac{\sum_{i=1}^{n}(S_i - R_i)}{\sum_{i=1}^{n} R_i} \times 100\% \tag{4}$$

$$MRE = \frac{\sum_{i=1}^{n}|S_i - R_i|}{\sum_{i=1}^{n} R_i} \tag{5}$$

in which S_i and R_i refer to the estimates of the SPPs and the observations from the reference datasets, respectively, and n is the total number of events involved in the analysis. *RB* reflects the extent to which the SPPs under/overestimate precipitation, while *MRE* provides an overall assessment, accounting for the potential offset in *RB* when computing the average. For both indices, the optimal value is 0 and the smaller absolute value indicates a better performance of the SPPs.

Peak-related properties consist of peak ratio (P_r, %) and time to peak (P_t, %), representing the magnitude and timing of event peak, respectively, defined as:

$$P_r = \frac{D_m}{D} \times 100\% \tag{6}$$

$$P_t = \frac{t_m - 1}{T - 1} \times 100\% \tag{7}$$

in which D_m is the precipitation depth (mm) at the peak hour and t_m denotes the time (h) from the event onset to the peak intensity in the event. The performance of the SPPs in estimating peak-related properties against the reference datasets was evaluated using scatter plot analysis.

3.3. Delineation of subregions with homogeneous characteristics

To analyze the collective impact of climate and land surface properties on the performance of the SPPs, a k-means clustering algorithm was employed to delineate subregions with homogeneity when accounting for factors such as climate conditions (averaged precipitation and temperature, based on Köppen climate classification, Fig. 1a, b), vegetation conditions (NDVI, Fig. 1c), terrain features (elevation, slope and aspect, Fig. 1d, e, f) and surface soil texture (percentage of sand, silt and clay, Fig. 1g, h, i). The optimal number of clusters was determined using the Silhouette Score method, which identifies the configuration that maximizes within-cluster cohesion and between-cluster separation, thereby ensuring a balance between spatial heterogeneity and interpretability (Aytaç, 2020).

To quantify the influence of each environmental factor on SPP accuracy, the concept of relative mutual information (RMI) was introduced (Ning et al., 2022). The mutual information $I(X_i, Y)$ between each environmental factor X_i and accuracy metric $Y$is computed by:

$$I(X_i, Y) = H(X_i) + H(Y) - H(X_i, Y) \tag{8}$$

in which, $H(X_i)$ and $H(Y)$ denote marginal entropy of the environmental factor and the accuracy metric, respectively, and $H(X_i, Y)$ is their joint entropy. These entropies are defined as:

$$H(X) = -\int p(x)\log p(x)\, dx \tag{9}$$

$$H(Y) = -\int p(y)\log p(y)\, dx \tag{10}$$

$$H(X, Y) = -\int p(x,y)\log p(x,y)\, dxdy \tag{11}$$

where $p(x)$, $p(y)$ and $p(x,y)$ denote the marginal density of X, Y and their joint density respectively. The mutual information values were then normalized within each subregion to derive the RMI of each factor:

$$w_i = \frac{I(X_i, Y)}{\sum_{i=1}^{n} I(X_i, Y)} \tag{12}$$

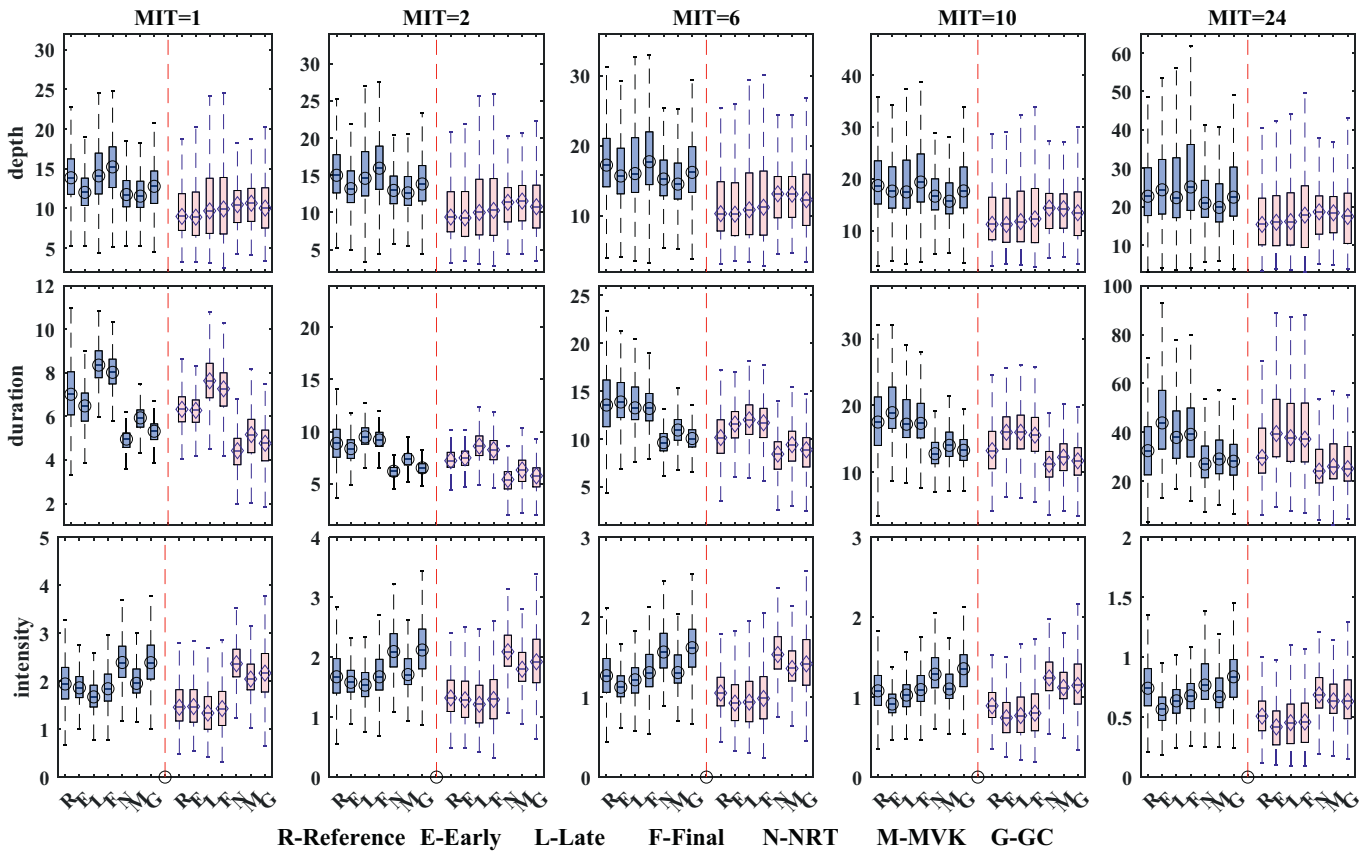

Fig. 3. Boxplots of the mean values of the three event properties (depth, duration, intensity) estimated by the GPM SPPs and reference datasets. The blue are results comparing to the gauge data, and red are results comparing to CLDAS. (For interpretation of the references to colour in this figure legend, the reader is referred to the web version of this article.)

in which, w_i denotes the RMI of the environmental factor *i*. It ranges from 0 to 1, with higher values indicating stronger influence on the SPPs' performance.

4. Results

4.1. Nationwide analysis of the property means of precipitation events identified by the SPPs

Two reference datasets (site observations and CLDAS grid data) were employed to evaluate the GPM SPPs separately. A nationwide analysis of the mean property values of all precipitation events were initially conducted (Fig. 3), and the extent of over/underestimations was also assessed (Fig. 4), considering all grid cells over the entire country. A "good agreement" was considered for a grid cell if the over/underestimation of the mean event property value was within 25 %, and a nationwide "satisfactory" performance on capturing this property was suggested by more than 60 % of the grid cells exhibiting a good agreement. The validation results against rain gauge and CLDAS datasets showed good consistency. Overall, the SPPs from IMERG and GSMaP demonstrated satisfactory and comparable abilities in discerning precipitation depth, despite some over/underestimations. Although Early tended to have more underestimations (Fig. 3), it exhibited a higher percentage of "good agreement" nationwide within the IMERG system, especially for MIT $\leq$2 h (>75 %) (Fig. 4). It indicated that Early well captured the precipitation depth for more grid cells within the whole area, compared to Late and Final. GC within GSMaP system presented a slight better performance than NRT and MVK. As for the mean precipitation duration, IMERG products showed clear overestimations while GSMaP products exhibited noticeable underestimations (Fig. 3–4). It can also be observed that IMERG products were superior for shorter MITs whereas GSMaP appeared to be better for longer MITs (MIT $\geq$ 6 h) In accordance to the performances of SPPs on identifying the mean precipitation depth and duration, the mean precipitation intensity was found to be underestimated by the IMERG products, while being overestimated by GSMaP. IMEGR products demonstrated higher percentages of "good agreement" compared to GSMaP for identifying precipitation intensity, especially for shorter MITs. For both event duration and intensity, it was interesting to note that the gauge-corrected versions in both systems did not perform better than their near/post real-time versions. Early presented the least discrepancies within IMERG system for shorter MITs, and MVK revealed its superiority among GSMaP products regardless of MIT values. In general, the influence of increasing MIT was relatively more pronounced for the estimation of mean event duration by the GPM SPPs compared to that of depth and intensity.

4.2. Detectability of precipitation events by the SPPs

The CLDAS datasets were only used for assessing detectability of precipitation events by the GPM SPPs, since the rain gauges identified an insufficient number of precipitation events ($\leq$50, compared to over 300 in CLDAS). Fig. 5 presents the detectability indices (i.e. POD, FAR, CSI) for all the SPPs. Generally, they all exhibited better performances for longer MITs ($\geq$ 6 h). With regard to POD, GSMaP products were slightly better than IMERG for longer MITs, whereas they displayed comparably poorer performance when MIT $\leq$ 2 h. Early was slightly inferior to Late and Final for shorter MITs, and Final showed relatively distinct superiority for longer MITs. Among the GSMaP products, MVK achieved the highest POD (for longer MITs) while the gauge-corrected version (GC) was unexpectedly the worst. IMERG products were more effective in

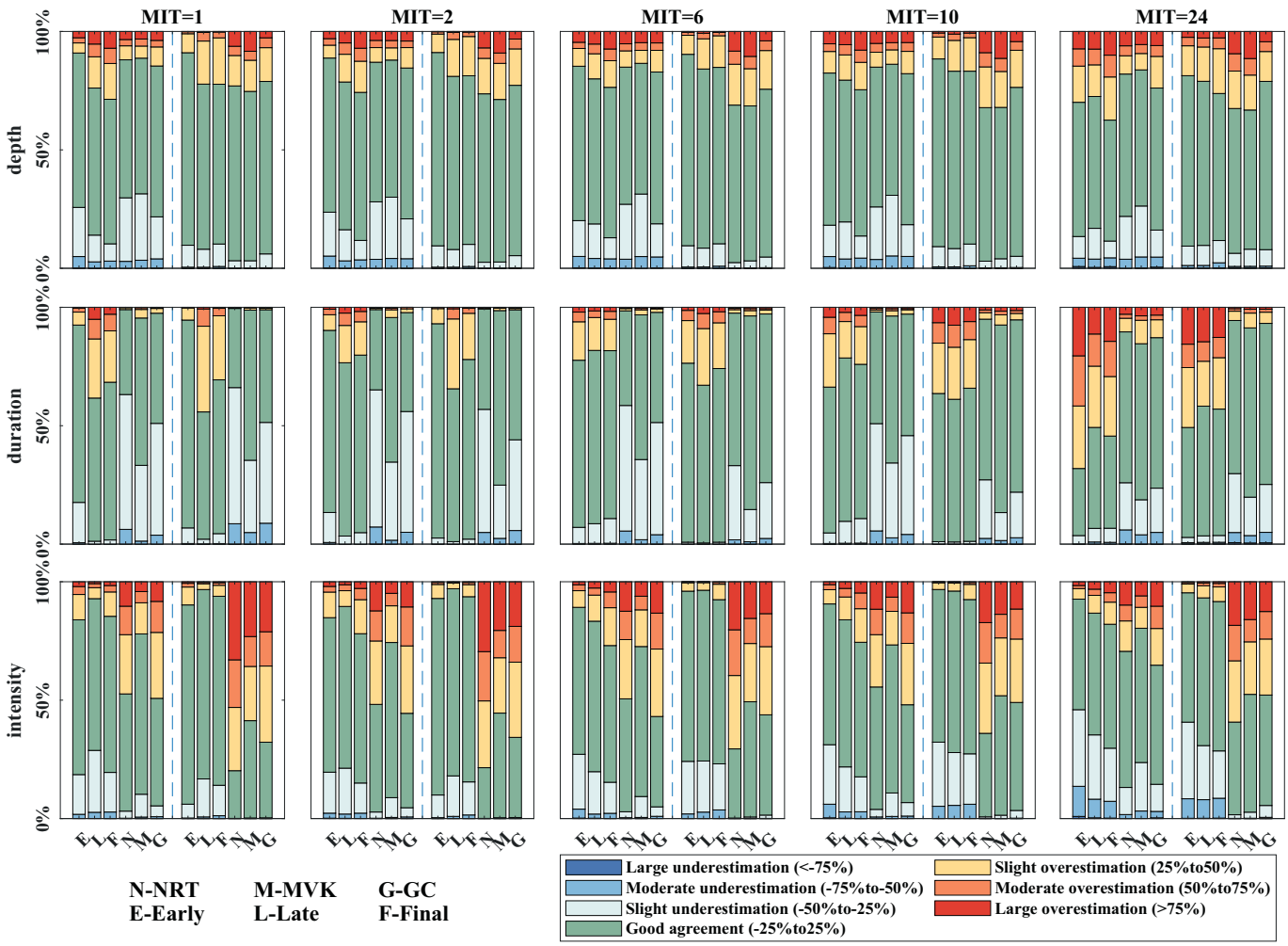

Fig. 4. Stacked bars of the relative errors of three properties (depth, duration and intensity) for the GPM SPPs. The left half are the results against site data, and the right are the results against CLDAS.

avoiding false alarms compared to GSMaP products. Late and GC displayed the lowest FAR in their respective system. The CSI of the IMEGR products was marginally higher than that of GSMaP for longer MITs, while the two systems had similar performances for shorter MITs. Overall, the detectability of all the SPPs was enhanced with an increase in MIT, evidenced by higher POD and CSI and lower FAR. It was also noted that substantial improvement was detected when MIT increased from 2 to 6 h, with POD_{p50} (the median value of POD) rising from 0.20 to 0.22 to 0.55–0.63, and FAR_{p50} decreasing from 0.72 to 0.75 to 0.48–0.52.

The spatial distribution of the three indices for all the SPPs is depicted in Fig. 6, Fig. S1 and Fig. S2. Better performances were observed in central and eastern China, indicated by higher POD and CSI, and lower FAR, while the coastal regions exhibited the most substantial improvements with increasing MIT. The increase in POD for IMERG products was less pronounced compared to GSMaP products when MIT exceeded 6 h. Nonetheless, all products were inadequate in detecting precipitation events (POD <0.2) in western China, particularly the Tibetan Plateau region (Fig. 1). IMERG products displayed higher POD in southern and eastern China, whereas GSMaP was more effective in the southwest. In terms of FAR, IMERG products were superior to GSMaP in northern and western China but were slightly inferior in the southern regions. As for CSI, the outperformance of IMERG over GSMaP was evident in eastern China. Within the IMERG system, Final performed marginally better than the near/post real-time products as reflected in the POD values, especially in southwest China. For GSMaP, NRT and MVK showed more desirable performance in the northwest compared to GC, while GC was slightly better in detecting precipitation events than NRT and MVK along the coastal regions, particularly when MIT ≥10 h, achieving POD >0.8 and FAR <0.2.

4.3. Evaluation of the SPPs in characterizing the event properties

The deviation between the precipitation events detected by the reference data and the SPPs were further analyzed to assess the reliability of SPPs. Only the events detected by both reference datasets (gauge-based and CLDAS data) and SPPs were considered, to avoid overestimation of the bias with high FAR. Probability density function (PDF) curves were constructed to illustrate the distribution of the relative bias (RB) on precipitation depth, duration and intensity against gauge data and CLDAS, as shown in Fig. 7 and Fig. 8, respectively. Besides, scatter plots of peak ratio (P_r) and time to peak (P_t) of precipitation events detected by the SPPs and CLDAS data are presented in Fig. 9 and Fig.S3.

All SPPs demonstrated their capability in monitoring the depth of precipitation events, with RB evenly distributed around zero, especially for GSMaP products, which was in line with the results of nationwide analysis (Figs. 3, 4). Interestingly, Early was superior to Late and Final in the IMERG system for shorter MITs, with values of RB more concentrated to zero. Within the GSMaP system, GC outperformed NRT and MVK in capturing precipitation depth, especially for longer MITs. IMERG and GSMaP revealed their strengths in detecting precipitation

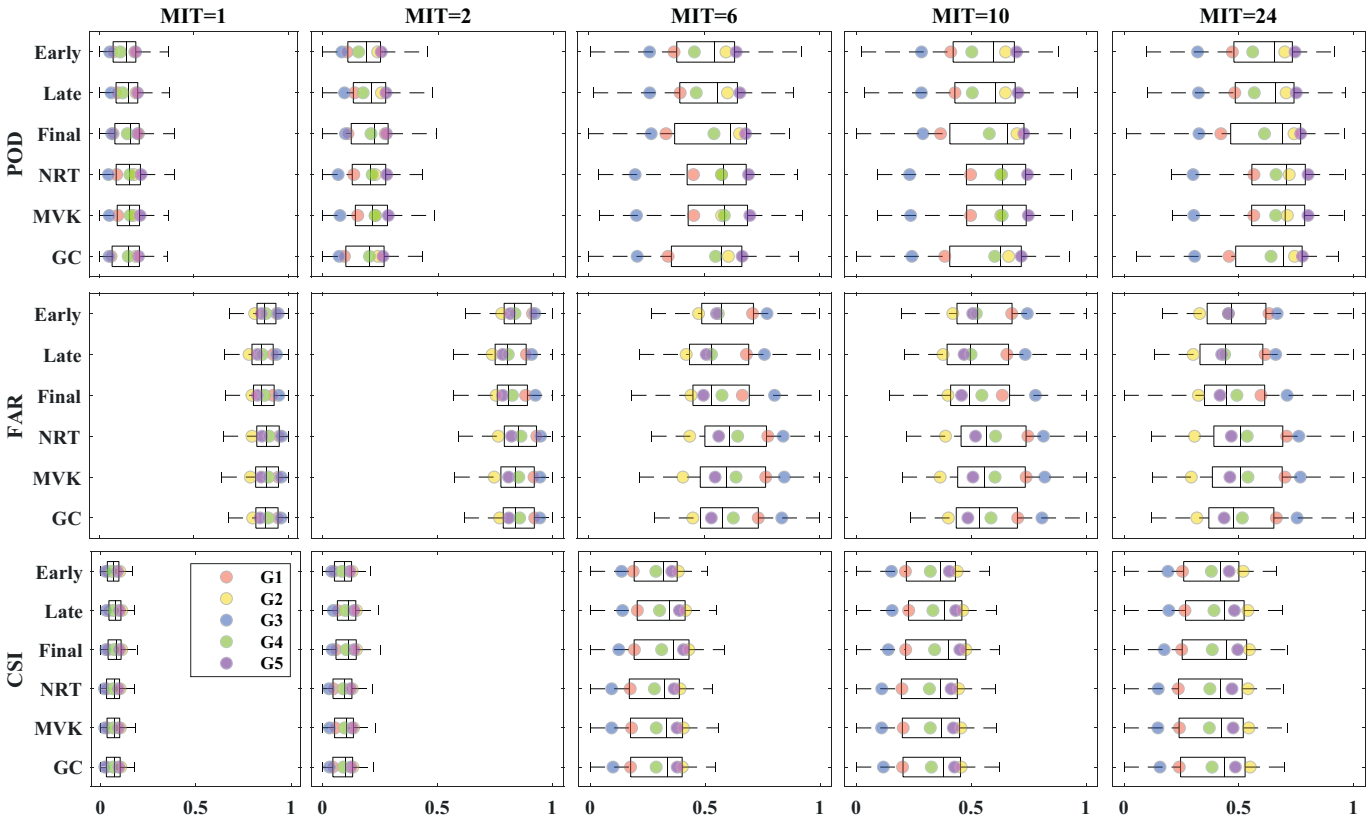

Fig. 5. Boxplots of POD, FAR and CSI for all the SPPs. The colored dots represent the mean values of the index for five subregions of the study area.

intensity and duration, respectively. Generally, IMERG overestimated precipitation duration by 6–52 % for different MITs, while the underestimation by GSMaP was 1–35 % with a more confined range. On the other hand, IMERG underestimated precipitation intensity by 3–17 % across varied MIT values, whereas GSMaP products presented a larger dispersion of the bias, concentrating to 4–27 % against site observations, and to 22–39 % against CLDAS. It is worth noting that MVK and Early performed the best in capturing precipitation duration and intensity within GSMaP and IMERG respectively, and the superiority of Early was more evident for shorter MITs, especially when evaluated with gauge data. Overall, the increase of MIT deteriorated the efficiency of these SPPs in characterizing precipitation duration while the impact was not significant for capturing precipitation depth and intensity, which was consistent with the nationwide analysis of the property means (Fig. 4). In terms of peak-related properties, IMERG products generally underestimated the peak ratio, whereas GSMaP products exhibited an overall overestimation (Fig. 9). Although IMERG products appeared to be less effective in detecting precipitation event duration, they demonstrated better capability of capturing the timing of peak intensity, especially for shorter MITs (Fig.S3). GSMaP products tended to overestimate time to peak, whereas their performance got improved with the increase of MIT. Early and MVK consistently outperformed the other two products within each system in estimating the peak magnitude, especially for shorter MITs (Fig. 9, Fig.S3).

The spatial distribution of RB for precipitation event properties identified by SPPs was also analyzed against CLDAS datasets (Fig. S4, S5, 10) and gauge measurements (Fig. S6, S7, 11), respectively. The results based on the two reference datasets exhibited similar spatial patterns. Specifically, the IMERG products overestimated precipitation depth in eastern China by 20 % ~ 60 %, while the overestimation by Early was less compared to the other two products, especially for shorter MITs. Some underestimations of precipitation depth by the IMERG products were detected in the western area, with the bias of Final more confined to the northwestern corner of China. NRT and MVK in the GsMAP system underestimated precipitation depth in some areas of southern China, while clear overestimations were observed in the northern region, particularly for the northwestern area. In contrast, the gauge-corrected version GC tended to underestimate precipitation depth in the northwestern China, showing a similar behavior with IMERG Final. In terms of precipitation duration and intensity, IMERG and GsMAP performed distinctly different. Overestimations of precipitation duration by IMERG products were observed for the whole study area (up to over 100 % for western China for longer MITs while 13 % ~ 57 % for eastern part), whereas GsMAP products underestimated duration by 5 % ~ 36 % for most of the area, particularly for shorter MITs. Accordingly, the IMERG SPPs appeared to underestimate precipitation intensity for a large proportion of the study area except for southern China, regardless of MIT. A nationwide overestimation of precipitation intensity by GsMAP products was observed, expect for some underestimations in the south for MVK and in northwestern regions for GC.

All the SPPs performed worse in the western area compared to the east. It should be noted that blank fields in the graphs for MIT $\leq$6 h denote the absence of precipitation events detected simultaneously by CLDAS and SPPs (Fig. S4, S5, 10), suggesting a less satisfactory performance of GSMaP products with more blank grids. However, the number of blank cells clearly decreased and diminished with the increase of MIT. The influence of increasing MIT was relatively noticeable for precipitation duration, with an overall reduced underestimation by GSMaP while an exacerbated overestimation by IMERG, particularly in western region. Notably, the gauge-corrected versions of the SPPs (Final and GC) did not show consistently better performance on characterizing each precipitation event property. Specifically, Early overestimated precipitation depth and duration in eastern China to the smallest extent within the IMERG system, especially for shorter MITs. Moreover, overestimation of precipitation intensity was more evident for Final in the northwestern China, compared with Early and Late. As for GSMaP

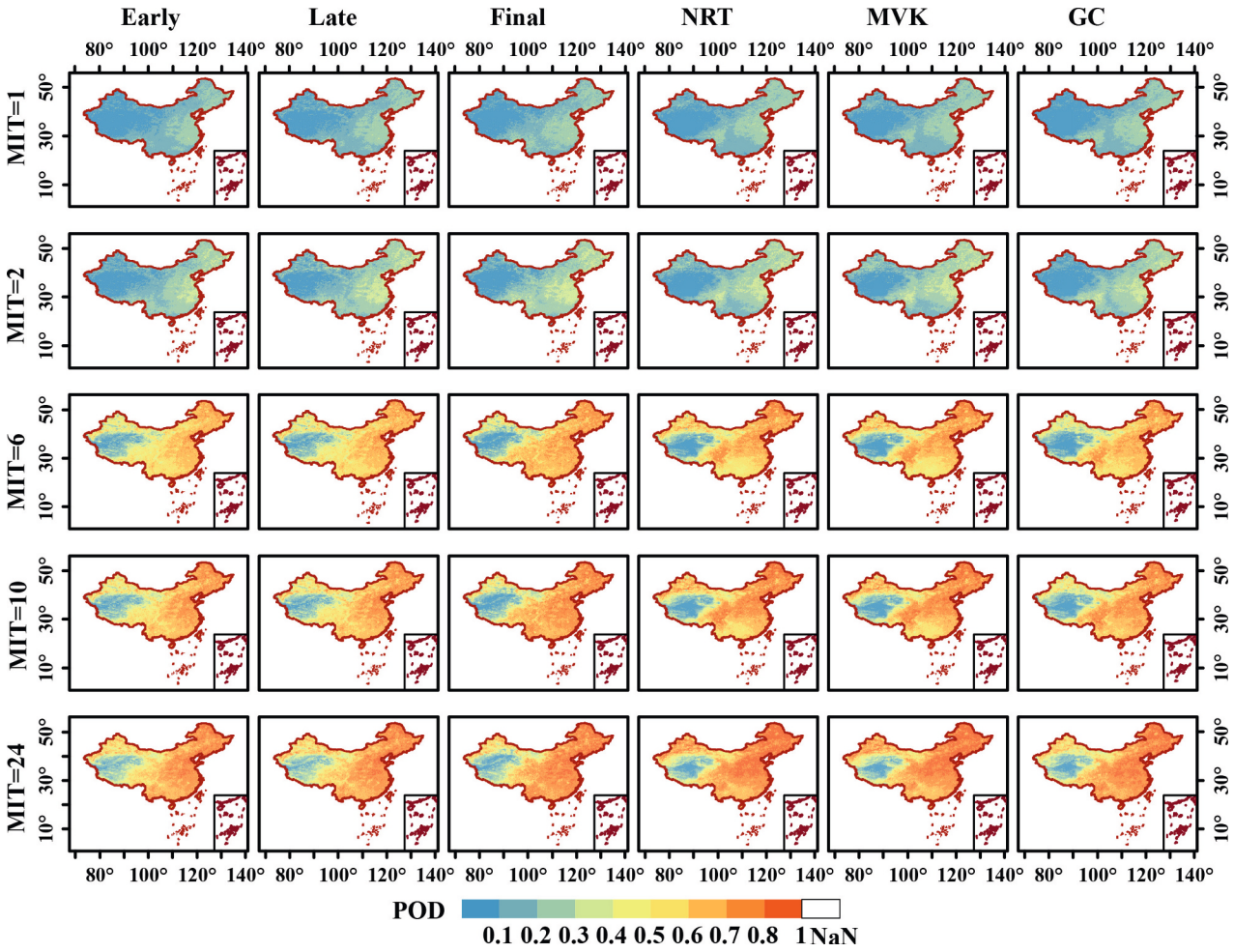

Fig. 6. The distribution of POD of the GPM SPPs against CLDAS datasets. See the Supplement for maps of the other two detectability indices.

products, despite greater overestimations of depth in western China, MVK exhibited its superiority in depicting event duration in northeastern China and intensity in southern region, regardless of MIT.

4.4. *Performance of the SPPs for subregions with homogeneity*

Five subregions with homogeneity when accounting for climate and land surface factors were generated using the K-means clustering algorithm (Fig. 1k). The regions identified were northwest region (G1), south China (G2), western plateau (G3), western steep-slope region (G4), and northeastern region (G5). The G1 region is predominantly desert climate (BWk), featured by higher temperatures, lower elevations, and less complex terrain, compared to other regions (G3 and G4) in northwestern China. The Tibet Plateau, identified as a separate region, the G3 region, is characterized by a tundra climate (ET) with low temperature and high altitudes. Region G4, covering the remaining western area, is subject to similar climatic conditions to the G3 region but having relatively higher precipitation, denser vegetation, and different landscape and soil properties. Eastern China was divided into two subregions, G2 and G5. The G2 region is characterized by a warm temperate climate, including a year-round humid climate (Cfb) and a climate with dry winters and hot summers (Cwa), both represented by higher NDVI and percentage of clay compared to other regions. Region G5 is subject to a snow climate, consisting of a climate with dry winters and hot summers (Dwa) and one with dry cold winters and cool summers (Dwc). Region G5 is featured by lower NDVI and a larger percentage of sand.

Fig. 5 presents the mean values of indices (i.e. POD, FAR and CSI) that used to assess the detectability of these SPPs for each subregion. In general, the best performance (highest CSI) for all SPPs was observed in G2, followed by G5, G4, G1 and G3 regardless of the MIT criteria, though the highest POD was noted in the G5 region (Fig. 5). The IMERG SPPs consistently outperformed GSMaP products with a relatively higher CSI value across all subregions, whereas this advantage diminished with decreasing MIT. Within the IMERG system, Final showed a higher POD than Early and Late except in the G1 region, where the gauge-corrected version GC of GSMaP also had a lower POD than NRT and MVK. Among the IMERG products, the lowest FAR was observed in Late except for in the G1 and G5 region. For the GSMaP products, MVK generally had a higher FAR than GC, while that was not the case for G2, regardless of MIT.

Fig. 12 displays the mean MRE of precipitation event properties detected by the SPPs against CLDAS in each subregion. In terms of their capacity in capturing precipitation depth, all the SPPs were relatively more effective in G4 and G5 while showing limited ability in G2 for shorter MITs, and G3 for longer MITs. Compared with GSMaP, the IMERG products had a better performance in the G1 and G4 region but was less efficient in the G2 region. Within the IMERG system, Final showed superiority in G1 and G5 while Early performed better for the other subregions. For the GSMaP products, MVK achieved the best performance in the G2 region, while GC was superior in G1 and G5. With respect to precipitation duration, all the SPPs were relatively inferior in the G3 region compared to the other subregions. Importantly, the capability of the GsMAP products did not vary substantially across subregions only except for G3, whereas IMERG products performed relatively better in G4 and G5. Notably, the IMERG products showed nearly equal capability in identifying precipitation event intensity for all

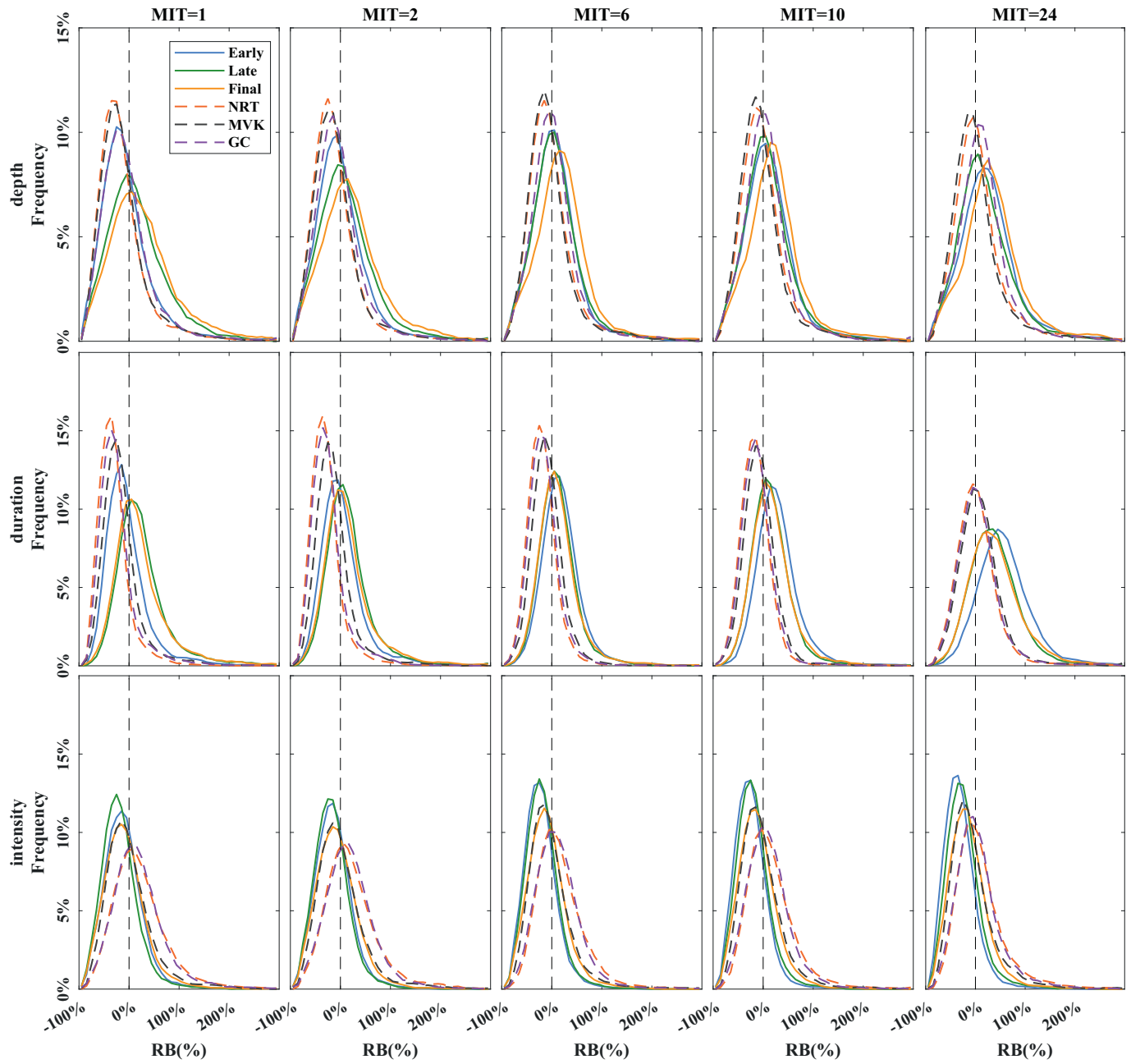

Fig. 7. Distribution of the relative bias of precipitation event properties (depth, duration and intensity) detected by the GPM SPPs against the gauge data.

subregions, regardless of the MIT, while for GSMaP, MVK tended to be more effective, except for the G1 region, where GC exhibited better behavior.

5. Discussion

5.1. Influence of MIT on the performance of the SSPs

This study observed that the amount and properties of precipitation events captured by the GPM SPPs were MIT-dependent (Fig. 3), being consistent with the findings in previous studies (Brasil et al., 2022; Dunkerley, 2008). Moreover, a pronounced enhancement in detectability was observed when MIT increased from 2 to 6 h, with only small differences for MIT $\geq$6 or $\leq$ 2 h. Phased sensitivity to MIT values has also been detected by gauge-based studies, which reported a clear independence among precipitation events identified by MIT values of 1, 10 and 24 h, whereas strong correlations among those derived from MIT values of 6, 8, and 10 h (He et al., 2022; Lemos et al., 2023). Despite that applying different MIT thresholds could provide a more comprehensive understanding of SPPs' effectiveness in precipitation characterization, an MIT of 1 h, 6 h and 24 h is recommended here as being adequate for the evaluation of SPPs.

The detectability of SPPs, as indicated by POD, FAR and CSI, was in general enhanced with increased values of MIT (Fig. 5–6, Fig. S1-S2). Precipitation events that were delineated using longer MITs tended to have a longer duration, thus our finding was in line with the better detectability of SPPs when analyzed at coarser temporal resolution (Chen et al., 2020b; Xu et al., 2019; Yuan et al., 2019) in China (Chen et al., 2020b) or for specific regions (Li et al., 2021a; Lu et al., 2020; Shi et al., 2021). However, the three detectability indices of all SPPs at shorter MITs were not as good as those in the existing hourly evaluation studies, which might be due to the possibility of amalgamating

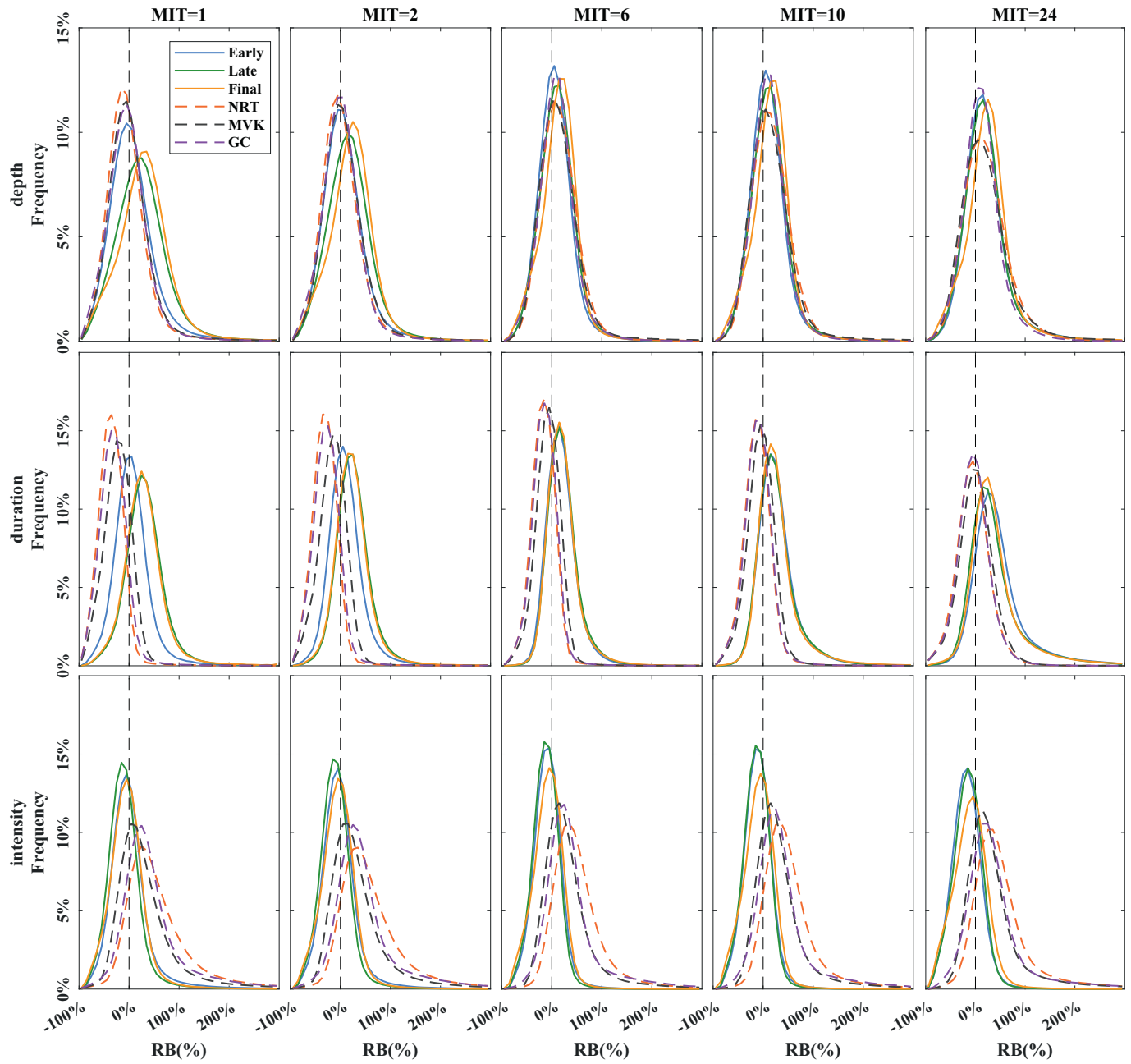

Fig. 8. Distribution of the relative bias of precipitation event properties (depth, duration and intensity) detected by the GPM SPPs against the CLDAS data.

consecutive precipitation events into a single event in the event-based analysis (Fig. 2). The range and spatial distribution of these indices at longer MITs were comparable to daily-scale studies in China (Zhou et al., 2020) and to a global extent (Chen et al., 2020b). When MIT increased, precipitation depth and duration became progressively larger for both the SPPs and the reference precipitation data, as indicated by the studies analyzing ground-based observations using different MITs (Dunkerley, 2015; Molina-Sanchis et al., 2016). In this study, precipitation duration was more remarkably overestimated by the IMERG products with a larger MIT (Fig. 7–8, Fig.S5), indicating their limitation in the identification of rain/no-rain periods, as also evidenced by the larger FAR at fixed-timescale evaluations (Chen et al., 2020b), especially for light rainfall (Li et al., 2021c).

In fact, selection of the MIT criterion relied on the intention of application using precipitation datasets (Dunkerley, 2008, 2015; Molina-Sanchis et al., 2016). In this study, all the GPM SPPs exhibited satisfactory detectability when MIT $\geq$6 h. Given that an MIT of 6 h has been widely adopted in many hydrological applications, such as runoff generation analysis, landslides and soil erosion monitoring (Brasil et al., 2022; Hirschberg et al., 2021), desirable detectability of precipitation events by the GPM SPPs is particularly important for establishing early warnings of rainfall-induced hazards, even though precipitation duration and intensity might not be perfectly captured.

5.2. *Event-based insights: different SPP from GPM has its own strength*

A large number of fixed-time validation studies have indicated that GSMaP products are inferior to IMERG in capturing precipitation in mainland China (Chen et al., 2020b; Lu and Yong, 2018; Zhou et al., 2020). However, the analysis presented here has revealed distinct advantages of each system in identifying precipitation characteristics. GSMaP SPPs appeared to be more capable of characterizing

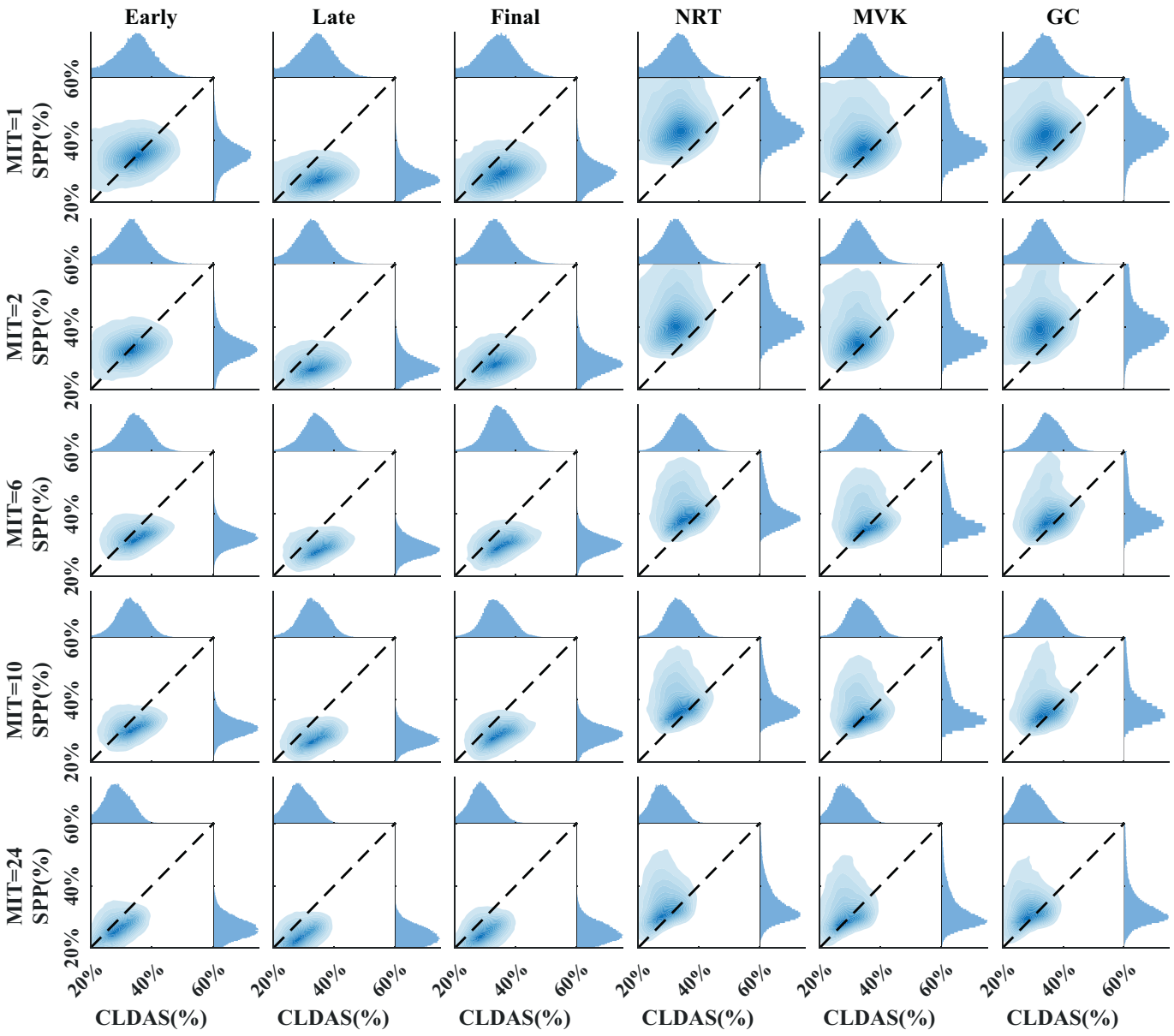

Fig. 9. Scatter plot of peak ratio detected by the GPM SPPs against CLDAS. See the Supplement for the scatter plot of time to peak.

precipitation event duration, while IMERG products excelled in capturing precipitation intensity (Fig. 7–8). In contrast to previous hourly evaluations which reported an overestimation of precipitation intensity by IMERG (Tang et al., 2020; Wang et al., 2020a, 2020b), a general underestimation by IMERG products was observed in this study. This inconsistency can be attributed to differences in the definition of precipitation intensity, which is defined as the average hourly depth in hourly studies, rather than the average depth over the event duration in our analysis. We found that the IMERG products tended to overestimate event duration, likely due to their limited ability to capture inter-event intervals, thus resulting in underestimated intensity. In terms of event peak properties, we observed an underestimation of peak ratio along with an overestimation of time to peak detected by IMERG, and delayed occurrence of maximum precipitation within a day was similarly revealed in the hourly evaluation of IMERG by Wang et al. (2023).

As for the detectability of the GPM SPPs, GSMaP products slightly excelled in accurately detecting the occurrence of precipitation events with higher POD values, while IMERG tended to be more effective in avoiding false alarms, reflected by lower FAR (Fig. 5–6, S1). The POD values and its spatial distribution from this study were consistent with those from hourly evaluations (Chen et al., 2020b; Tang et al., 2016; Zhang et al., 2023), whereas the behavior in terms of FAR was different. Hourly evaluations found a higher FAR for IMERG, whereas this study observed a consistently lower FAR for IMERG regardless of MIT. Precipitation events detected by IMERG products tended to have longer duration and lower intensity. In this regard, the larger FAR reported in fixed-timescale evaluations was likely due to the overestimation of precipitation duration rather than a deficiency of IMERG in discerning non-existent precipitation events. Therefore, event-based evaluation could provide a more comprehensive view of their detectability.

We assessed the performance of SPPs using different MIT thresholds and revealed varying effectiveness in capturing precipitation events, which could guide the selection of SPPs for specific purposes. The IMERG products tended to better avoid detecting non-existent precipitation events and be more capable of capturing event peak magnitude and timing, suggesting their potential for application in real-time warnings of hydrometeorological hazards. GSMaP products exhibited higher POD and appeared to be more effective in identifying event depth and duration, especially for longer MITs. It indicated that GSMaP is likely to be more suitable for longer-term climate and water resources analysis.

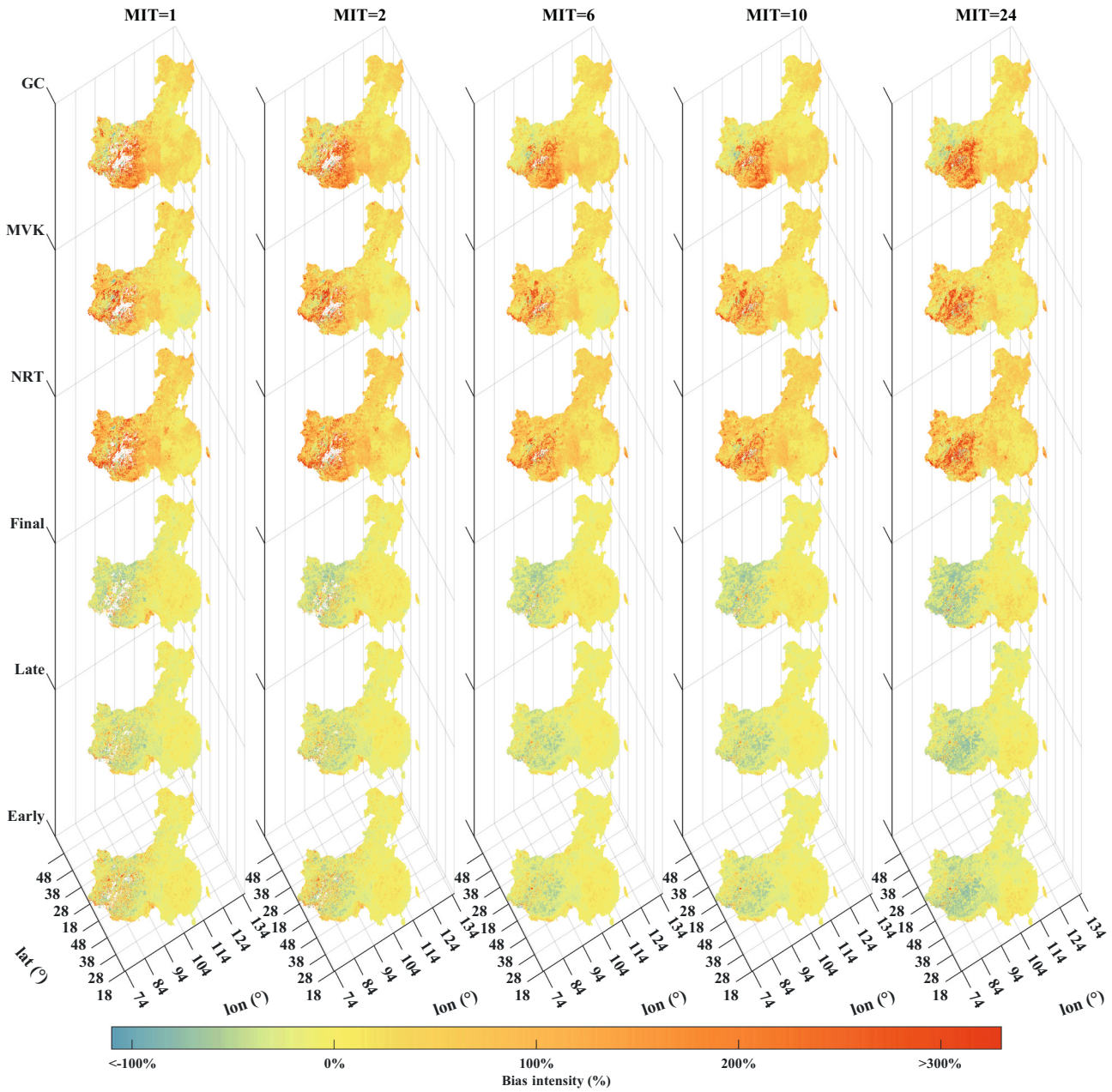

Fig. 10. The spatial distribution of relative bias of precipitation intensity detected by the GPM SPPs against CLDAS. See the Supplement for maps of the relative bias for precipitation depth and duration.

Previous fixed-timescale evaluation studies generally found that gauge-corrected versions of GPM SPPs outperformed near/post real-time products (Yuan et al., 2019; Zhou et al., 2020), while the event-based analysis of this study suggested superiority of near/post real-time SPPs in some aspects. Within the IMERG system, Final outperformed Early and Late in detecting precipitation events with higher POD and CSI regardless of MIT, which was consistent with the results from hourly or daily validation studies (Lu et al., 2020; Tang et al., 2020; Yang et al., 2020). However, Final did not show a pronounced improvement over near/post real-time products in either detectability or characterizing event properties. Specifically, IMERG Late stood out by its capability to minimize false alarms, achieving the lowest FAR, which was also observed in the fixed-timescale evaluations (Tang et al., 2020; Yang et al., 2020; Zhou et al., 2020) as well as typhoon route tracing (Yu et al., 2020) and analysis of extreme rainfall events (Zhou et al., 2021). Moreover, the event-based analysis of this study unexpectedly revealed the outperformance of IMERG Early in capturing the features of precipitation events (duration, intensity, peak ratio and time to peak) for shorter MITs (Figs. 4, 7–9). The capability of Early in capturing sudden and short-duration precipitation events, especially the peak properties, could be particularly valuable for providing timely information and early warnings, which could be potentially used for flood forecasting in small to medium watersheds, given its latency of only 4 h.

Among the three products in the GSMaP system, GC did not consistently outperform NRT as expected, particularly in terms of detectability (Fig. 5–6). Previous fixed-timescale studies demonstrated the superiority of GSMaP GC over its near/post real-time products, with higher correlation coefficients and lower biases against in-situ measurements (Lu and Yong, 2020; Palharini et al., 2020; Zhu and Liu, 2024). However, our analysis found that even though GC performed better in identifying precipitation depth, it underestimated duration and overestimated precipitation intensity more remarkably than MVK. This might be

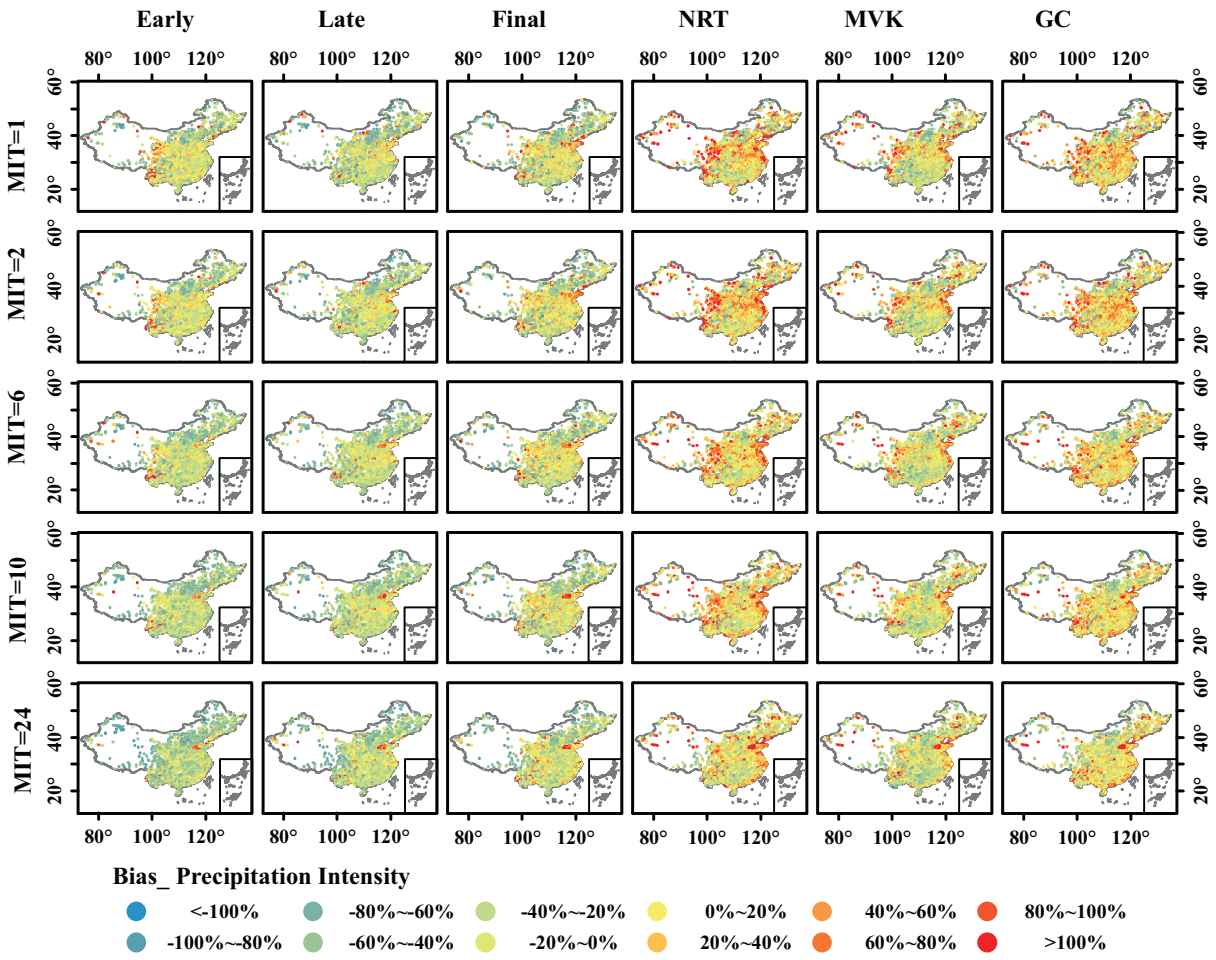

Fig. 11. The spatial distribution of relative bias of precipitation intensity detected by the GPM SPPs against gauge data. See the Supplement for maps of the relative bias for precipitation depth and duration.

attributed to its correction process, which primarily adjusted the cumulative precipitation depth at fixed intervals. The reliability of GC significantly relied on the quality and gauge density of the CPC precipitation data, suggesting that inadequacies in gauge coverage or data quality could diminish its effectiveness in capturing precipitation (Yuan et al., 2019), such as its performance in the subregion of G1 (Fig. 5). Instead, MVK demonstrated its superiority, as also reported in several fixed-timescale studies (Chen et al., 2020b; Shi et al., 2021; Tan et al., 2018), both in the detection (POD) and characterization of precipitation events (duration and intensity), especially for longer MITs. The outperformance of MVK over GC suggested the possible inefficiency of current corrections, especially in sparsely gauged regions. The limitation of gauge-based correction could be also underscored by the less significant improvement of gauge-corrected products in IMERG due to the coarser temporal resolution of the correction datasets (Arshad et al., 2021; Omranian et al., 2018; Shawky et al., 2019). Given the underlying inadequacy of gauge data regarding spatial coverage, data precision and completeness, traditional algorithms when combined with other satellite observations might serve as a good alternative for correcting real-time versions of the SPP. For instance, the Kalman Filter (KF) which was applied in the MVK product proved its efficiency by improving the performance of the SPPs through integration of different data sources, e.g. model and radar precipitation data (Sokol, 2009), satellite radiance data (Zhu et al., 2019), and satellite soil moisture data (Yin and Zhan, 2018). With the emergence of more advanced algorithms (e.g. Bayesian method, Hybrid method, machine learning algorithms), the SPP correction could possibly be achieved despite the absence of a dense rain gauge network.

5.3. *Interaction of multiple factors in influencing the performance of SPPs*

The six GPM SPPs exhibited a similar spatial pattern of detectability, showing an increasing trend from west to east, with the best performance in southern China, indicating regional-dependency of the capability of SPP in detecting precipitation events. RMI was then introduced to quantify the importance of each factor, and the results for POD, FAR and relative bias of precipitation properties are shown in Fig. 13 and Fig. S8–9 (results for different MIT thresholds showed minimal variation, therefore the results for MIT = 10 h are presented as representative). NDVI and DEM were identified as the main factors influencing detectability for the whole study area, while a potentially interactive effect of these factors on the detectability of the SSPs could also be observed (Fig. 13, S8). All the SPPs presented relatively poor performance in the western part of China, especially in the G3 region, where the high elevation has been identified as a factor limiting the behavior of SPPs by a number of studies (Chen et al., 2019; Derin et al., 2019; Fang et al., 2019; Zhang et al., 2018). The lower POD in high-altitude regions resulted from the limited capacity of SPPs in detecting shallow orographic precipitation events, which were prevalent in these areas (Fig. 13, Chen et al., 2019; Prakash et al., 2018). Nevertheless, higher POD values were observed in the G4 region, which also featured by high altitude levels, but with steeper slopes, denser vegetation, and heterogeneous soil textures (Fig. 1). Increased terrain complexity is normally associated with poorer behavior of SPPs (Amjad et al., 2020; Dayal et al., 2023; Tang et al., 2016), while in densely vegetated areas the SPPs tended to have better performance due to a wet condition (Chen et al., 2016; Dayal et al., 2023). Compared with G3 region, the influence of

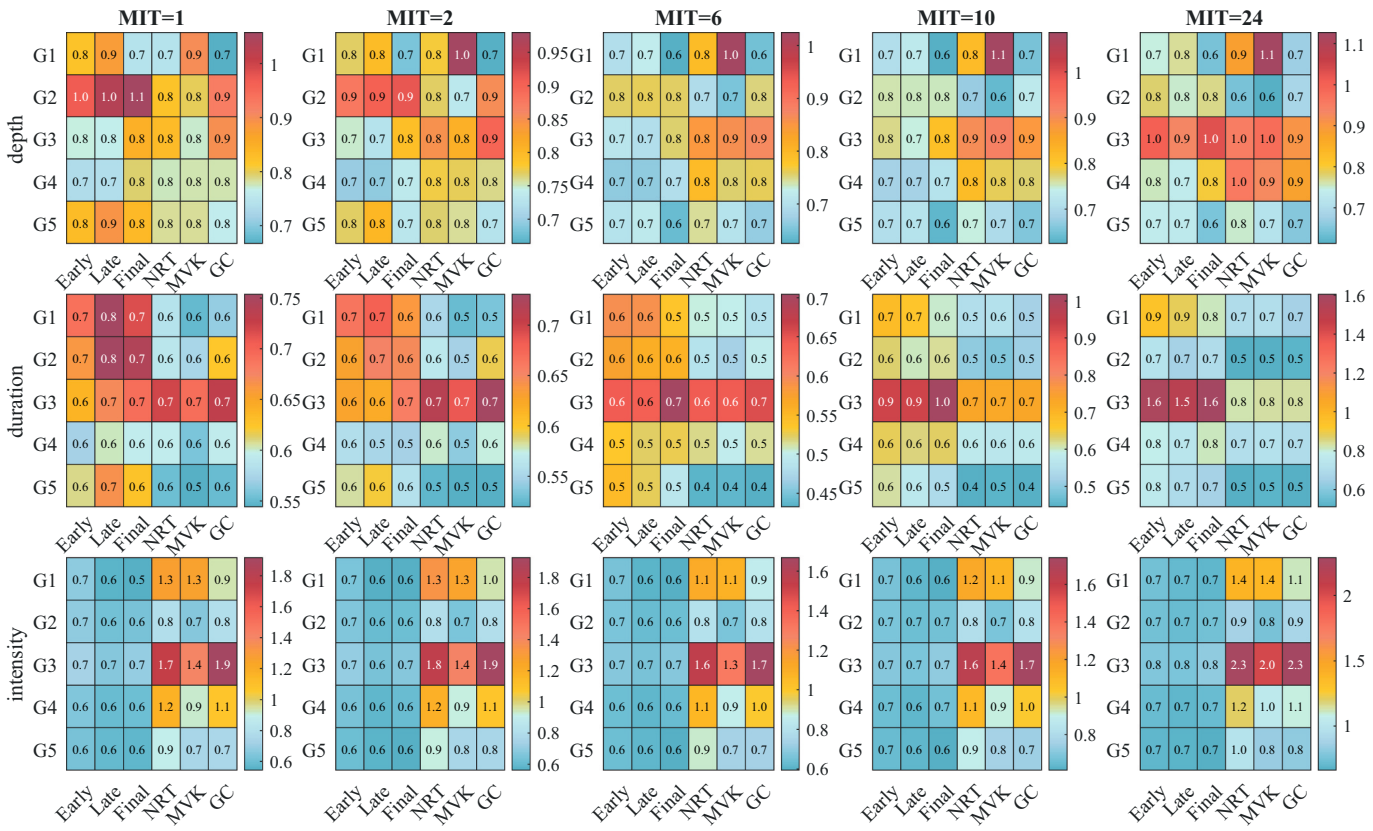

Fig. 12. The mean MRE of event properties detected by the GPM SPPs against CLDAS for the subregions.

NDVI as indicated by RMI was more evident in the G4 region, which potentially led to a more satisfactory detectability of the SPPs. However, Chen et al. (2016) found that there was no correlation between NDVI and POD, which was likely due to their analysis being confined to summertime with stable vegetation conditions. Chen et al. (2020a) also identified a strong correlation between the behavior of SPPs and elevation rather than with NDVI. The reason for the less dominant influence of elevation in region G4 could be that segmenting continuous precipitation records into discrete events might diminish the significance of the correlation. Additionally, factors influencing the correlation between the SPPs and in-situ measurements might not be the primary effect on precipitation event detectability. Satisfactory detectability of SPPs in the G1 region (Bwk climate) was found, while it was in contrast to the findings by Ma et al. (2019), who reported poor behavior of IMERG products in Bwk climate. Factors apart from the climate, like simpler terrain conditions, might compensate for the negative impact of climate with a near-equal contribution to the detectability of SPPs (Fig. 13, S8).

Compared with western China (i.e. the G1, G3, G4 regions), the relatively denser vegetation cover predominantly led to the preferable POD values, while the less satisfactory detectability in G5 compared to G2 was likely subject to its drier condition (Fig. 13), which was consitent with the findings from previous studies (Amjad et al., 2020; Jiang and Bauer-Gottwein, 2019). Despite a possible decrease in POD with increasing aridity (Chen and Wen, 2023), our results suggested that humidity was not the only factor for the detectability of SPPs. Temperature, which significantly effect on precipitation formation and air convection conditions (Behrangi et al., 2016), might also have an influence on detectability. In this regard, the milder temperature variations in the G5 region were possibly associated with the better detectability of the SPPs (Fig. 13, S8). The observed impact of land surface temperature on downscaling of SPP underscores the critical role of temperature on the accuracy of SPPs (Jing et al., 2016). A clear decrease in FAR was observed in more sophisticated landscapes, as also found in previous studies (Chen et al., 2016; Derin et al., 2019; Gebregiorgis et al., 2012). Specifically, steep slopes together with less dense vegetation collectively led to a lower FAR in region G4, as compared to region G3 (Figs. 1, 5, S1, S8). Additionally, both the gentler slope and humid climate condition contributed to the lower FAR in region G2, when comparing to region G5. Distinct behavior of the subregions suggested that the impact of a specific factor on SPP detectability could differ across regions (Fig. 13, S8).

The performance of the GPM SPPs was also subject to external factors with different sensitivity. For instance, a slight superiority in detectability of IMERG over GSMaP was observed in the G3 region, possibly due to the enhanced stability of the new GMI sensor, which operated across an extended frequency range (10–183 GHz) and performed better for regions of higher elevations, compared with other inputs, including TMI, AMSR2, SSMIS and AMSU-A/MHS (Chen et al., 2019), potentially leading to less sensitivity of the IMERG products towards terrian factors (Fig. 13). Chen and Wen (2023) found that integrating observations from PWM and IR sensors could effectively reduce topographical influence on the behavior of SPPs. However, GSMaP products exhibited a higher POD than IMERG in region G4, also characterized by high elevation, implying that factors beyond elevation dominated the performance of GSMaP products (Fig. 13). We assumed vegetation condition played a more important role than elevation, hinted by the outperformance of GSMaP over IMERG in region G2, which has higher levels of NDVI.

The partial incorporation of GMI into the GSMaP system likely

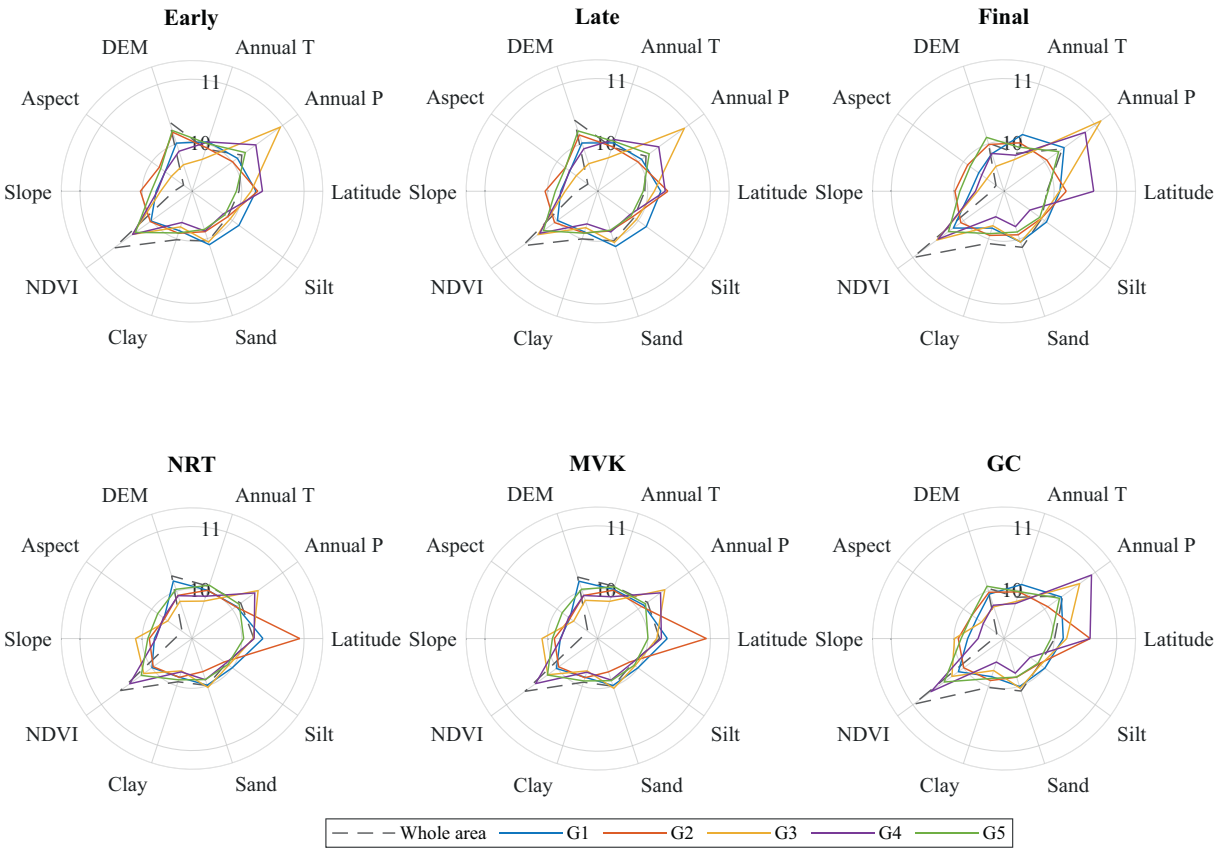

Fig. 13. RMI of different environmental factors on POD under MIT = 10 h for the subregions. See the Supplement for FAR and relative bias of precipitation depth, duration and intensity.

affected how these SPPs responded to underlying environmental factors (Chen et al., 2019). Previous studies claimed that the interpretation of IR resulted in a better detectability of IMERG than GSMaP. However, IR has typically presented a relatively high ratio of false fraction compared with other components (Chen et al., 2019; Sui et al., 2020) while a lower FAR for IMERG was observed than for GSMaP in this event-based study. The relatively lower percentage of false fraction of GMI in the IMERG system possibly contributed to its better ability of avoiding false alarms. The IR technology effectively captured precipitation from convection (Chen and Wen, 2023; Chen et al., 2023), which might have led to the superiority of IMERG over GSMaP in precipitation detection in southern China (G5), where convective precipitation events are more frequent.

Although the SPPs from both GPM systems over/underestimated precipitation event properties to a varying extent, biases were consistently much more pronounced in western China compared to the eastern region. The spatial distribution of RB for all three precipitation properties corresponded closely with climate patterns (Fig. 10–11, S4-S7). In the relatively humid regions (G2 and G5), SPPs were more reliable in detecting precipitation events, which was consistent with the reduced biases reported in humid (Fang et al., 2019; Jiang and Bauer-Gottwein, 2019; Peng et al., 2021) and semi-humid regions (Chen et al., 2019). Region G2 exhibited larger biases than G5, due to its distinctly variable slopes and greater variation in precipitation (Fig. S9), since SPPs tended to have unsatisfactory performance in regions with complex terrain (Chen et al., 2019; Chen and Wen, 2023). Dayal et al. (2023) identified a positive correlation between random SPPs errors and NDVI, whereas we conversely observed smaller biases in southern China (G5) with the highest NDVI, which might suggest the dominant influence of humid climate conditions on the performance of the SPPs in the G5 region (Fig. S9).

A number of studies have claimed that a specific factor (e.g. topography, climate, vegetation) is the primary driver of SPP accuracy (Chen and Wen, 2023; Dayal et al., 2023; Sui et al., 2020; Zhu et al., 2021), whereas interacting effect of multiple factors has been rarely pointed out. Our study revealed the potential collective impact of different factors on the performance of SPP via delineating subregions with homogeneity when accounting for a range of external factors. Such insight could be enlightening for establishing downscaling or real-time correction strategies for SPPs, especially for increasingly used machine learning methods, which in essence explore the connections between ancillary variables. For instance, it is recommended that the processing of satellite precipitation be tailored for the specific subregions. Specifically, a uniform model can be applied for those subregions with homogeneous characteristics, especially in absence of dense gauge network (Choubin et al., 2019; Wang et al., 2020a, 2020b).

6. Conclusion

In this study, we evaluated and intercompared the performance of six satellite precipitation products (SPPs) of the GPM mission (both IMERG and GSMaP) over China from an event-based perspective, with a specific focus on their effectiveness in detecting precipitation events and capturing event properties (i.e. depth, duration, intensity, peak ratio and time to peak). The minimum inter-event time (MIT) approach with different threshold values (i.e. 1, 2, 6, 10, 24 h) was applied to delineate precipitation events for the SSPs and the reference data (site observations and CLDAS datasets). The integrating impact of various external factors on the performance of SPPs was also explored by subregion division using the K-means cluster method. The conclusions drawn from this study are as follows.

(1) IMEGR and GSMaP exhibited distinct strengths in avoiding false alarms (lower FAR) and detecting the existent precipitation events (higher POD), respectively. IMERG performed better in identifying precipitation intensity and event peak, whereas GSMaP products were more effective in estimating event depth and duration, especially for longer MITs. The overestimation of event duration by IMERG products was possibly due to their tendency to capture precipitation in a continuous pattern, which contrasted with explanations from fixed-timescale evaluations that IMERG was ineffective at avoiding false alarms. The different superiority of IMEGR and GSMaP suggested their potential for timely hydrological forecasting and longer-term water resources analysis, respectively.

(2) Near/post real-time products demonstrated their outperformance over gauge-corrected versions in certain aspects. Early exhibited its superiority in characterizing the event-based precipitation properties within the IMERG system, especially for smaller MITs ($\leq$ 2 h). As for the GSMaP system, MVK performed better than NRT and GC in capturing precipitation duration and intensity, and also exceled in detectability, with highest POD. The unexpected strengths of near/post real-time products in the two systems suggested their potential for rainfall monitoring and early warning of associated hazards, and the possible effectiveness of gauge-free satellite retrieval algorithms.

(3) Vegetation condition and terrain were in general the two main factors influencing SPPs' behavior. Complex terrain had an adverse impact on the performance of all the SPPs, whereas dense vegetation, humid weather conditions and mild temperature variation, could potentially act as tradeoffs, integrally leading to a desirable detectability. The performance of SPPs was subject to an interplay of multiple external factors and the sensitivity of SPPs' behavior to a specific factor varied across regions.

The results of this study identified the comparative strengths of the GPM SPPs (IMERG versus GSMaP, and near-real-time products versus gauge-corrected ones) in capturing precipitation events, which is expected to bring new insights for practical applications and contribute to the ongoing development and refinement of the SPPs.

CRediT authorship contribution statement

Meng Cao: Writing – original draft, Visualization, Validation, Investigation, Formal analysis, Data curation, Conceptualization. **Min Chen:** Writing – review & editing, Supervision, Conceptualization. **Jeffrey Walker:** Writing – review & editing.

Declaration of competing interest

The authors declare that they have no known competing financial interests or personal relationships that could have appeared to influence the work reported in this paper.

Acknowledgements

This work was supported by the National Natural Science Foundation of China (No.41807513).

Appendix A. Supplementary data

Supplementary data to this article can be found online at https://doi.org/10.1016/j.atmosres.2025.108231.

Data availability

Data will be made available on request.

References

Administration, C.M., 2017. CMA Land Data Assimilation System Forcing Data. Accessed 6 July 2021. http://www.nmic.cn/data/cdcdetail/dataCode/NAFP_CLDAS2.0_NRT.html.

Amjad, M., Yilmaz, M.T., Yucel, I., Yilmaz, K.K., 2020. Performance evaluation of satellite- and model-based precipitation products over varying climate and complex topography. J. Hydrol. 584.

Anjum, M.N., Ding, Y., Shangguan, D., Ahmad, I., Ijaz, M.W., Farid, H.U., Yagoub, Y.E., Zaman, M., Adnan, M., 2018. Performance evaluation of latest integrated multi-satellite retrievals for Global Precipitation Measurement (IMERG) over the northern highlands of Pakistan. Atmos. Res. 205, 134–146.

Arshad, M., Ma, X., Yin, J., Ullah, W., Ali, G., Ullah, S., Liu, M., Shahzaman, M., Ullah, I., 2021. Evaluation of GPM-IMERG and TRMM-3B42 precipitation products over Pakistan. Atmospheric Research 249.

Ayat, H., Evans, J.P., Sherwood, S., Behrangi, A., 2021. Are storm characteristics the same when viewed using merged surface radars or a merged satellite product? J. Hydrometeorol. 22, 43–62.

Aytaç, E., 2020. Unsupervised learning approach in defining the similarity of catchments: Hydrological response unit based k-means clustering, a demonstration on Western Black Sea Region of Turkey. Int. Soil Water Conserv. Res. 8, 321–331.

Beck, H.E., Vergopolan, N., Pan, M., Levizzani, V., van Dijk, A., Weedon, G.P., Brocca, L., Pappenberger, F., Huffman, G.J., Wood, E.F., 2017. Global-scale evaluation of 22 precipitation datasets using gauge observations and hydrological modeling. Hydrol. Earth Syst. Sci. 21, 6201–6217.

Behrangi, A., Christensen, M., Richardson, M., Lebsock, M., Stephens, G., Huffman, G.J., Bolvin, D., Adler, R.F., Gardner, A., Lambrigtsen, B., Fetzer, E., 2016. Status of high-latitude precipitation estimates from observations and reanalyses. J. Geophys. Res.-Atmos. 121, 4468–4486.

Berg, P., Moseley, C., Haerter, J.O., 2013. Strong increase in convective precipitation in response to higher temperatures. Nat. Geosci. 6, 181–185.

Bi, Z.Y., Sun, S.L., Shen, H.Y., Liu, Y., Ren, Y.J., Li, J.J., Lin, B., 2022. Systematic assessment of GPM IMERG V06 precipitation products with dense rain gauge observations over Zhejiang Province, China. Int. J. Climatol. 42, 9471–9493.

Blenkinsop, S., Fowler, H.J., Barbero, R., Chan, S.C., Guerreiro, S.B., Kendon, E., Lenderink, G., Lewis, E., Li, X.-F., Westra, S., Alexander, L., Allan, R.P., Berg, P., Dunn, R.J.H., Ekstrom, M., Evans, J.P., Holland, G., Jones, R., Kjellstrom, E., Klein-Tank, A., Lettenmaier, D., Mishra, V., Prein, A.F., Sheffield, J., Tye, M.R., 2017. The INTENSE project: Using observations and models to understand the past. Present and future of sub-daily rainfall extremes. In: 17th EMS Annual Meeting / European Conference for Applied Meteorology and Climatology, pp. 117–126. Dublin, Ireland.

Brasil, J.B., Guerreiro, M.S., Andrade, E.M.D., Palacio, H.A.D., Medeiros, P.H.A., Ribeiro, J.C., 2022. Minimum rainfall inter-event time to separate rainfall events in a low latitude semi-arid environment. Sustainability 14.

Chen, H.Q., Wen, D.B., 2023. Dependency of errors for four global reanalysis and satellite precipitation estimates on four crucial factors. Atmos. Res. 296.

Chen, M., Shi, W., Xie, P., Silva, V.B.S., Kousky, V.E., Higgins, R.W., Janowiak, J.E., 2008. Assessing objective techniques for gauge-based analyses of global daily precipitation. J. Geophys. Res.-Atmos. 113.

Chen, Z., Qin, Y., Shen, Y., Zhang, S., 2016. Evaluation of global satellite mapping of precipitation project daily precipitation estimates over the Chinese mainland. Adv. Meteorol. 2016, 1–15.

Chen, H., Yong, B., Gourley, J.J., Liu, J., Ren, L., Wang, W., Hong, Y., Zhang, J., 2019. Impact of the crucial geographic and climatic factors on the input source errors of GPM-based global satellite precipitation estimates. J. Hydrol. 575, 1–16.

Chen, C., Li, Z., Song, Y., Duan, Z., Mo, K., Wang, Z., Chen, Q., 2020a. Performance of multiple satellite precipitation estimates over a typical arid mountainous area of China: spatiotemporal patterns and extremes. J. Hydrometeorol. 21, 533–550.

Chen, H., Yong, B., Shen, Y., Liu, J., Hong, Y., Zhang, J., 2020b. Comparison analysis of six purely satellite-derived global precipitation estimates. J. Hydrol. 581.

Chen, H.Q., Wen, D.B., Du, Y.A., Xiong, L.Y., Wang, L.Y., 2023. Errors of five satellite precipitation products for different rainfall intensities. Atmos. Res. 285.

Chiaravalloti, F., Brocca, L., Procopio, A., Massari, C., Gabriele, S., 2018. Assessment of GPM and SM2RAIN-ASCAT rainfall products over complex terrain in southern Italy. Atmos. Res. 206, 64–74.

Choubin, B., Khalighi-Sigaroodi, S., Mishra, A., Goodarzi, M., Shamshirband, S., Ghaljaee, E., Zhang, F., 2019. A novel bias correction framework of TMPA 3B42 daily precipitation data using similarity matrix/homogeneous conditions. Sci. Total Environ. 694.

Dayal, D., Pandey, A., Gupta, P.K., Himanshu, S.K., 2023. Multi-criteria evaluation of satellite-based precipitation estimates over agro-climatic zones of India. Atmos. Res. 292.

Demaria, E.M.C., Rodriguez, D.A., Ebert, E.E., Salio, P., Su, F., Valdes, J.B., 2011. Evaluation of mesoscale convective systems in South America using multiple satellite products and an object-based approach. J. Geophys. Res.-Atmos. 116.

Derin, Y., Anagnostou, E., Berne, A., Borga, M., Boudevillain, B., Buytaert, W., Chang, C.-H., Chen, H., Delrieu, G., Hsu, Y.C., Lavado-Casimiro, W., Manz, B., Moges, S., Nikolopoulos, E.I., Sahlu, D., Salerno, F., Rodriguez-Sanchez, J.-P., Vergara, H.J., Yilmaz, K.K., 2019. Evaluation of GPM-era global satellite precipitation products over multiple complex terrain regions. Remote Sens. 11.

Devine, S.M., Steenwerth, K.L., O'Geen, A.T., 2021. A regional soil classification framework to improve soil health diagnosis and management. Soil Sci. Soc. Am. J. 85, 361–378.

Donoghue, S., Furley, P.A., Stuart, N., Haggis, R., Trevaskis, A., Lopez, G., 2019. The nature and spatial variability of lowland savanna soils: improving the resolution of soil properties to support land management policy. Soil Use Manag. 35, 547–560.

Dunkerley, D., 2008. Identifying individual rain events from pluviograph records: a review with analysis of data from an Australian dryland site. Hydrol. Process. 22, 5024–5036.
Dunkerley, D.L., 2010. How do the rain rates of sub-event intervals such as the maximum 5-and 15-min rates (I-5 or I-30) relate to the properties of the enclosing rainfall event? Hydrol. Process. 24, 2425–2439.
Dunkerley, D., 2012. Effects of rainfall intensity fluctuations on infiltration and runoff: rainfall simulation on dryland soils, Fowlers Gap, Australia. Hydrol. Process. 26, 2211–2224.
Dunkerley, D., 2015. Intra-event intermittency of rainfall: an analysis of the metrics of rain and no-rain periods. Hydrol. Process. 29, 3294–3305.
Fang, J., Yang, W., Luan, Y., Du, J., Lin, A., Zhao, L., 2019. Evaluation of the TRMM 3B42 and GPM IMERG products for extreme precipitation analysis over China. Atmos. Res. 223, 24–38.
Freitas, E.D.S., Coelho, V.H.R., Xuan, Y., Melo, D.D.C.D., Gadelha, A.N., Santos, E.A., Galvao, C.D.O., Ramos Filho, G.M., Barbosa, L.R., Huffman, G.J., Petersen, W.A., Almeida, C.D.N., 2020. The performance of the IMERG satellite-based product in identifying sub-daily rainfall events and their properties. J. Hydrol. 589.
Gadelha, A.N., Coelho, V.H.R., Xavier, A.C., Barbosa, L.R., Melo, D.C.D., Xuan, Y., Huffman, G.J., Petersen, W.A., Almeida, C.d.N., 2019. Grid box-level evaluation of IMERG over Brazil at various space and time scales. Atmos. Res. 218, 231–244.
Gebregiorgis, A.S., Tian, Y., Peters-Lidard, C.D., Hossain, F., 2012. Tracing hydrologic model simulation error as a function of satellite rainfall estimation bias components and land use and land cover conditions. Water Resour. Res. 48.
Han, Z., Shi, Y., Wu, J., Xu, Y., Zhou, B., 2019. Combined dynamical and statistical downscaling for high-resolution projections of multiple climate variables in the Beijing-Tianjin-Hebei Region of China. J. Appl. Meteorol. Climatol. 58, 2387–2403.
Hanel, M., Maca, P., 2014. Spatial variability and interdependence of rain event characteristics in the Czech Republic. Hydrol. Process. 28, 2929–2944.
He, S.J., Wang, Z.L., Wang, D.G., Liao, W.L., Wu, X.S., Lai, C.G., 2022. Spatiotemporal variability of event-based rainstorm: the perspective of rainfall pattern and concentration. Int. J. Climatol. 42, 6258–6276.
Hirschberg, J., Badoux, A., McArdell, B.W., Leonarduzzi, E., Molnar, P., 2021. Evaluating methods for debris-flow prediction based on rainfall in an Alpine catchment. Nat. Hazards Earth Syst. Sci. 21, 2773–2789.
Hou, A.Y., Kakar, R.K., Neeck, S., Azarbarzin, A.A., Kummerow, C.D., Kojima, M., Oki, R., Nakamura, K., Iguchi, T., 2014. The global precipitation measurement mission. Bull. Am. Meteorol. Soc. 95, 701.
Hsu, K.L., Gao, X.G., Sorooshian, S., Gupta, H.V., 1997. Precipitation estimation from remotely sensed information using artificial neural networks. J. Appl. Meteorol. 36, 1176–1190.
Jiang, L., Bauer-Gottwein, P., 2019. How do GPM IMERG precipitation estimates perform as hydrological model forcing? Evaluation for 300 catchments across Mainland China. J. Hydrol. 572, 486–500.
Jing, W.L., Yang, Y.P., Yue, X.F., Zhao, X.D., 2016. A comparison of different regression algorithms for downscaling monthly satellite-based precipitation over North China. Remote Sens. 8.
Joyce, R.J., Janowiak, J.E., Arkin, P.A., Xie, P.P., 2004. CMORPH: a method that produces global precipitation estimates from passive microwave and infrared data at high spatial and temporal resolution. J. Hydrometeorol. 5, 487–503.
Katsiabani, K., Cartalis, C., Adaktilou, N., Mavrakis, A., Theocharatos, G., 2006. An assessment of the relationship of the vegetation and precipitation patterns in support of the estimation of drought episodes in Greece. In: Atlantic Europe Conference on Remote Imaging and Spectroscopy. Univ Cent Lancashire, Preston, ENGLAND (pp. 123-+).
Krueck, S., Joschko, M., Schultz-Sternberg, R., Kroschewski, B., Tessmann, J., 2006. A classification scheme for earthworm populations (Lumbricidae) in cultivated agricultural soils in Brandenburg, Germany. J. Plant Nutr. Soil Sci. 169, 651–660.
Kubota, T., Shige, S., Hashizurne, H., Aonashi, K., Takahashi, N., Seto, S., Hirose, M., Takayabu, Y.N., Ushio, T., Nakagawa, K., Wanami, K., Kachi, M., Okamoto, K.i., 2007. Global precipitation map using satellite-borne microwave radiometers by the GSMaP project: production and validation. IEEE Trans. Geosci. Remote Sens. 45, 2259–2275.
Kucera, P.A., Ebert, E.E., Turk, F.J., Levizzani, V., Kirschbaum, D., Tapiador, F.J., Loew, A., Borsche, M., 2013. Precipitation from space advancing earth system science. Bull. Am. Meteorol. Soc. 94, 365–375.
Kummerow, C., 1993. TRMM rainfall algorithm development. In: 13th Annual International Geoscience and Remote Sensing Symposium (IGARSS 93). Kogakuin Univ, Tokyo, Japan, pp. 419–420.
Lamjiri, M.A., Dettinger, M.D., Ralph, F.M., Guan, B., 2017. Hourly storm characteristics along the US West Coast: role of atmospheric rivers in extreme precipitation. Geophys. Res. Lett. 44, 7020–7028.
Lemos, F.C., Coelho, V.H.R., Freitas, E.D., Tomasella, J., Bertrand, G.F., Meira, M.A., Ramos, G.M., Fullhart, A., Almeida, C.D., 2023. Spatiotemporal distribution of precipitation and its characteristics under tropical atmospheric systems of Brazil: insights from a large sub-hourly database. Hydrol. Process. 37.
Lewis, E., Fowler, H., Alexander, L., Dunn, R., McClean, F., Barbero, R., Guerreiro, S., Li, X.-F., Blenkinsop, S., 2019. GSDR: a global sub-daily rainfall dataset. J. Clim. 32, 4715–4729.
Li, Q., Wei, J., Yin, J., Qiao, Z., Peng, W., Peng, H., 2021a. Multiscale comparative evaluation of the GPM and TRMM precipitation products against ground precipitation observations over Chinese Tibetan Plateau. Ieee J. Sel. Top. Appl. Earth Obs. Remote Sens. 14, 2295–2313.
Li, R., Wang, K., Qi, D., 2021b. Event-based evaluation of the GPM multisatellite merged precipitation product from 2014 to 2018 over China: methods and results. J. Geophys. Res.-Atmos. 126.
Li, X., Sungmin, O., Wang, N., Liu, L., Huang, Y., 2021c. Evaluation of the GPM IMERG V06 products for light rain over Mainland China. Atmos. Res. 253.
Li, D., Min, X., Xu, J., Xue, J., Shi, Z., 2022. Assessment of three gridded satellite-based precipitation products and their performance variabilities during typhoons over Zhejiang, southeastern China. J. Hydrol. 610.
Li, R.Z., Guilloteau, C., Kirstetter, P.E., Foufoula-Georgiou, E., 2023. How well does the IMERG satellite precipitation product capture the timing of precipitation events? J. Hydrol. 620.
Libertino, A., Sharma, A., Lakshmi, V., Claps, P., 2016. A global assessment of the timing of extreme rainfall from TRMM and GPM for improving hydrologic design. Environ. Res. Lett. 11.
Lu, D., Yong, B., 2018. Evaluation and hydrological utility of the latest GPM IMERG V5 and GSMaP V7 precipitation products over the Tibetan Plateau. Remote Sens. 10.
Lu, D., Yong, B., 2020. A preliminary assessment of the gauge-adjusted near-real-time GSMaP precipitation estimate over Mainland China. Remote Sens. 12.
Lu, H., Ding, L., Ma, Z., Li, H., Lu, T., Su, M., Xu, J., 2020. Spatiotemporal assessments on the satellite-based precipitation products from Fengyun and GPM over the Yunnan-Kweichow Plateau, China. Earth Space Sci. 7.
Ma, L., Zhao, L., Tian, L.-M., Yuan, L.-M., Xiao, Y., Zhang, L.-L., Zou, D.-F., Qiao, Y.-P., 2019. Evaluation of the integrated multi-satellite retrievals for global precipitation measurement over the Tibetan Plateau. J. Mt. Sci. 16, 1500–1514.
Maranan, M., Fink, A.H., Knippertz, P., Amekudzi, L.K., Atiah, W.A., Stengel, M., 2020. A process-based validation of GPM IMERG and its sources using a mesoscale rain gauge network in the West African forest zone. J. Hydrometeorol. 21, 729–749.
Mei, Y.W., Anagnostou, E.N., Nikolopoulos, E.I., Borga, M., 2014. Error analysis of satellite precipitation products in mountainous basins. J. Hydrometeorol. 15, 1778–1793.
Mei, Y.W., Nikolopoulos, E.I., Anagnostou, E.N., Zoccatelli, D., Borga, M., 2016. Error analysis of satellite precipitation-driven modeling of flood events in complex alpine terrain. Remote Sens. 8.
Molina-Sanchis, I., Lazaro, R., Arnau-Rosalen, E., Calvo-Cases, A., 2016. Rainfall timing and runoff: the influence of the criterion for rain event separation. J. Hydrol. Hydromech. 64, 226–236.
Nikolopoulos, E.I., Anagnostou, E.N., Borga, M., 2013. Using high-resolution satellite rainfall products to simulate a major flash flood event in Northern Italy. J. Hydrometeorol. 14, 171–185.
Ning, Y.W., Liang, G.H., Ding, W., Shi, X.G., Fan, Y.R., Chang, J.X., Wang, Y.M., He, B., Zhou, H.C., 2022. A mutual information theory-based approach for assessing uncertainties in deterministic multi-category precipitation forecasts. Water Resour. Res. 58.
Omranian, E., Sharif, H.O., Tavakoly, A.A., 2018. How well can global precipitation measurement (GPM) capture hurricanes? Case study: hurricane harvey. Remote Sens. 10.
Palharini, R.S.A., Vila, D.A., Rodrigues, D.T., Quispe, D.P., Palharini, R.C., de Siqueira, R. A., Afonso, J.M.D., 2020. Assessment of the extreme precipitation by satellite estimates over South America. Remote Sens. 12.
Peng, S.Z., Ding, Y.X., Liu, W.Z., Li, Z., 2019. 1 km monthly temperature and precipitation dataset for China from 1901 to 2017. Earth Syst. Sci. Data 11, 1931–1946.
Peng, J., Liu, T., Huang, Y., Ling, Y., Li, Z., Bao, A., Chen, X., Kurban, A., De Maeyer, P., 2021. Satellite-based precipitation datasets evaluation using gauge observation and hydrological modeling in a typical arid land watershed of Central Asia. Remote Sens. 13.
Pradhan, R.K., Markonis, Y., Godoy, M.R.V., Villalba-Pradas, A., Andreadis, K.M., Nikolopoulos, E.I., Papalexiou, S.M., Rahim, A., Tapiador, F.J., Hanel, M., 2022. Review of GPM IMERG performance: a global perspective. Remote Sens. Environ. 268.
Prakash, S., Mitra, A.K., AghaKouchak, A., Liu, Z., Norouzi, H., Pai, D.S., 2018. A preliminary assessment of GPM-based multi-satellite precipitation estimates over a monsoon dominated region. J. Hydrol. 556, 865–876.
Quintero, F., Krajewski, W.F., Mantilla, R., Small, S., Seo, B.C., 2016. A spatial-dynamical framework for evaluation of satellite rainfall products for flood prediction. J. Hydrometeorol. 17, 2137–2154.
Roversi, G., Pancaldi, M., Cossich, W., Corradini, D., Nguyen, T.T.N., Nguyen, T.V., Porcu, F., 2024. The extreme rainfall events of the 2020 typhoon season in Vietnam as seen by seven different precipitation products. Remote Sens. 16.
Salih, W., Epule, T.E., El Khalki, E.L., Ouatiki, H., Erraki, S., Achli, S., Chehbouni, A., 2024. A comprehensive assessment of satellite precipitation products over a semi-arid region: focus on extreme events. Nat. Hazards 120, 3037–3065.
Sharifi, E., Steinacker, R., Saghafian, B., 2018. Multi time-scale evaluation of high-resolution satellite-based precipitation products over northeast of Austria. Atmos. Res. 206, 46–63.
Shawky, M., Moussa, A., Hassan, Q.K., El-Sheimy, N., 2019. Performance Assessment of Sub-Daily and Daily Precipitation Estimates Derived from GPM and GSMaP Products over an Arid Environment. Remote Sensing 11.
Shen, Y., Pan, Y., Yu, J., Zhao, P., Zhou, Z., 2013. Quality assessment of hourly merged precipitation product over China. Trans. Atmos. Sci. 36, 37–46.
Shen, Y., Zhao, P., Pan, Y., Yu, J., 2014. A high spatiotemporal gauge-satellite merged precipitation analysis over China. J. Geophys. Res.-Atmos. 119, 3063–3075.
Shi, C., Xie, Z., Qian, H., Liang, M., Yang, X., 2011. China land soil moisture EnKF data assimilation based on satellite remote sensing data. Sci. China-Earth Sci. 54, 1430–1440.
Shi, J., Wang, B., Wang, G., Yuan, F., Shi, C., Zhou, X., Zhang, L., Zhao, C., 2021. Are the latest GSMaP satellite precipitation products feasible for daily and hourly discharge simulations in the Yellow River Source Region? Remote Sens. 13.

Sokol, Z., 2009. Effects of an assimilation of radar and satellite data on a very-short range forecast of heavy convective rainfalls. Atmos. Res. 93, 188–206.
Sui, X.X., Li, Z., Ma, Z.Q., Xu, J.T., Zhu, S.Y., Liu, H., 2020. Ground validation and error sources identification for GPM IMERG product over the Southeast Coastal Regions of China. Remote Sens. 12.
Sun, S., Shi, C., Pan, Y., Bai, L., Xu, B., Zhang, T., Han, S., Jiang, L., 2020. Applicability assessment of the 1998-2018 CLDAS multi-source precipitation fusion dataset over China. J. Meteorol. Res. 34, 879–892.
Tan, X.H., Yong, B., Ren, L.L., 2018. Error features of the hourly GSMaP multi-satellite precipitation estimates over nine major basins of China. Hydrol. Res. 49, 761–779.
Tang, G., Ma, Y., Long, D., Zhong, L., Hong, Y., 2016. Evaluation of GPM Day-1 IMERG and TMPA Version-7 legacy products over Mainland China at multiple spatiotemporal scales. J. Hydrol. 533, 152–167.
Tang, S., Li, R., He, J., Wang, H., Fan, X., Yao, S., 2020. Comparative evaluation of the GPM IMERG early, late, and final hourly precipitation products using the CMPA data over Sichuan Basin of China MDPI. Water 12.
Tapiador, F.J., Roca, R., Del Genio, A., Dewitte, B., Petersen, W., Zhang, F., 2019. Is precipitation a good metric for model performance? Bull. Am. Meteorol. Soc. 100, 223–234.
Tapiador, F.J., Marcos, C., Sancho, J.M., Santos, C., Núñez, J.A., Navarro, A., Kummerow, C., Adler, R.F., 2021. The September 2019 floods in Spain: an example of the utility of satellite data for the analysis of extreme hydrometeorological events. Atmos. Res. 257.
Ushio, T., Sasashige, K., Kubota, T., Shige, S., Okamoto, K.I., Aonashi, K., Inoue, T., Takahashi, N., Iguchi, T., Kachi, M., Oki, R., Morimoto, T., Kawasaki, Z.-I., 2009. A Kalman filter approach to the global satellite mapping of precipitation (GSMaP) from combined passive microwave and infrared radiometric data. J. Meteorol. Soc. Jpn 87A, 137–151.
Wang, W., Yin, S., Xie, Y., Nearing, M.A., 2019. Minimum inter-event times for rainfall in the eastern monsoon region of China. Trans. ASABE 62, 9–18.
Wang, Y.D., Kong, Y.F., Chen, H., Zhao, L., 2020a. Improving daily precipitation estimates for the Qinghai-Tibetan plateau based on environmental similarity. Int. J. Climatol. 40, 5368–5388.
Wang, H., Wang, L., He, J., Ge, F., Chen, Q., Tang, S., Yao, S., 2020b. Can the GPM IMERG hourly products replicate the variation in precipitation during the wet season over the Sichuan Basin, China? Earth Space Sci. 7.
Wang, Y., Miao, C., Zhao, X., Zhang, Q., Su, J., 2023. Evaluation of the GPM IMERG product at the hourly timescale over China. Atmos. Res. 285.
Xu, S., Wu, C., Wang, L., Gonsamo, A., Shen, Y., Niu, Z., 2015. A new satellite-based monthly precipitation downscaling algorithm with non-stationary relationship between precipitation and land surface characteristics. Remote Sens. Environ. 162, 119–140.
Xu, S., Shen, Y., Niu, Z., 2019. Evaluation of the IMERG version 05B precipitation product and comparison with IMERG version 04A over mainland China at hourly and daily scales. Adv. Space Res. 63, 2387–2398.
Yang, F., Lu, H., Yang, K., He, J., Wang, W., Wright, J.S., Li, C., Han, M., Li, Y., 2017. Evaluation of multiple forcing data sets for precipitation and shortwave radiation over major land areas of China. Hydrol. Earth Syst. Sci. 21, 5805–5821.
Yang, X., Lu, Y., Tan, M.L., Li, X., Wang, G., He, R., 2020. Nine-year systematic evaluation of the GPM and TRMM precipitation products in the Shuaishui River Basin in East-Central China. Remote Sens. 12.
Yin, J.F., Zhan, X.W., 2018. Impact of bias-correction methods on effectiveness of assimilating SMAP soil moisture data into NCEP global forecast system using the ensemble Kalman filter. IEEE Geosci. Remote Sens. Lett. 15, 659–663.
Yu, C., Hu, D., Liu, M., Wang, S., Di, Y., 2020. Spatio-temporal accuracy evaluation of three high-resolution satellite precipitation products in China area. Atmos. Res. 241.
Yu, C., Hu, D.Y., Di, Y.F., Wang, Y.C., 2021. Performance evaluation of IMERG precipitation products during typhoon Lekima (2019). J. Hydrol. 597.
Yuan, F., Zhang, L., Soe, K.M.W., Ren, L., Zhao, C., Zhu, Y., Jiang, S., Liu, Y., 2019. Applications of TRMM- and GPM-Era multiple-satellite precipitation products for flood simulations at sub-daily scales in a sparsely gauged watershed in Myanmar. Remote Sens. 11.
Zhang, C., Chen, X., Shao, H., Chen, S., Liu, T., Chen, C., Ding, Q., Du, H., 2018. Evaluation and intercomparison of high-resolution satellite precipitation EstimatesGPM, TRMM, and CMORPH in the Tianshan Mountain Area. Remote Sens. 10.
Zhang, Y., Huang, Y., Xu, H., Wang, S., Long, T., Zhao, Q., 2023. Evaluation of precipitation frequency and intensity as estimated by the GPM IMERG precipitation product at daily and hourly scales over the Tibetan Plateau. Atmosphere 14.
Zhou, Z., Guo, B., Xing, W., Zhou, J., Xu, F., Xu, Y., 2020. Comprehensive evaluation of latest GPM era IMERG and GSMaP precipitation products over mainland China. Atmos. Res. 246.
Zhou, C., Gao, W., Hu, J., Du, L., Du, L., 2021. Capability of IMERG V6 early, late, and final precipitation products for monitoring extreme precipitation events. Remote Sens. 13.
Zhu, S.L., Liu, Z.F., 2024. Comprehensive quantitative assessment of the performance of fourteen satellite precipitation products over Chinese mainland. Clim. Dyn. 62, 6799–6818.
Zhu, K.F., Xue, M., Pan, Y.J., Hu, M., Benjamin, S.G., Weygandt, S.S., Lin, H.D., 2019. The impact of satellite radiance data assimilation within a frequently updated regional forecast system using a GSI-based ensemble Kalman filter. Adv. Atmos. Sci. 36, 1308–1326.
Zhu, S.Y., Shen, Y., Ma, Z.Q., 2021. A new perspective for charactering the spatio-temporal patterns of the error in GPM IMERG over mainland China. Earth Space Sci. 8.